INVESTIGATING THE EFFECT OF SIZE SORTING ON THE VERTICAL VARIATION OF RAIN DROP SIZE DISTRIBUTIONS USING PARSIVEL DISDROMETERS AND WSR-88D RADARS DURING VORTEX-SE

by

Marcus Leon Terrell

A Thesis

Submitted to the Faculty of Purdue University

In Partial Fulfillment of the Requirements for the degree of

Master of Science

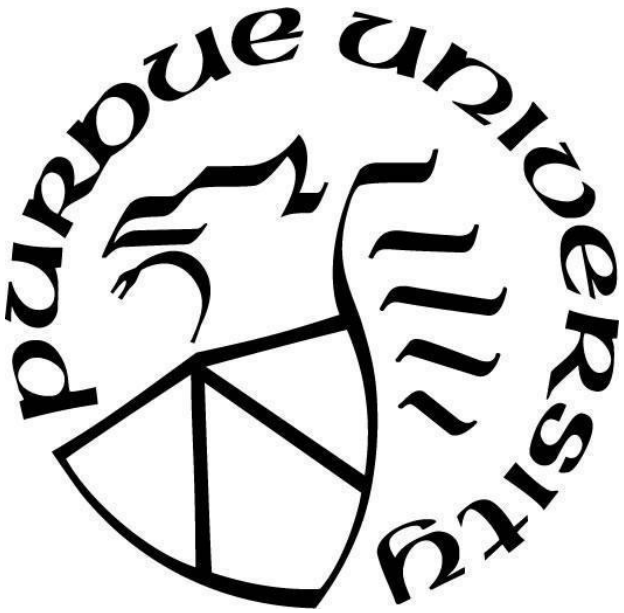

Department of Earth, Atmospheric, and Planetary Sciences

West Lafayette, Indiana

August 2021

THE PURDUE UNIVERSITY GRADUATE SCHOOL
STATEMENT OF COMMITTEE APPROVAL

Dr. Daniel T. Dawson II, Chair

Department of Earth, Atmospheric, and Planetary Sciences

Dr. Robin Tanamachi

Department of Earth, Atmospheric, and Planetary Sciences

Dr. Daniel Chavas

Department of Earth, Atmospheric, and Planetary Sciences

Approved by:

Dr. Daniel J. Cziczo

ACKNOWLEDGMENTS

First, I would like to thank the U.S. Navy for providing me with the opportunity to simultaneously instruct future naval officers and further my education in the graduate school. I would like to thank my wife, Mary, for her continued love, support, and allowing me to dedicate numerous hours towards my research and studies. I would like to thank my advisor, Daniel Dawson, for his patience, expertise, and guidance throughout my classes, entirety of my research, and the opportunity to work with him. His commitment and dedication to his team and severe storms has no bounds. I would also like to thank my committee members, Robin Tanamachi and Daniel Chavas, for their guidance throughout class and my thesis process. I am grateful for the students in the Atmospheric Science department for their patience, aid, and countless hours helping me with data analysis and coding.

My motivation for this project is centered on severe storms and size sorting of hydrometeors. Microphysical processes in severe convective storms are complex and difficult to observe, yet have crucial impacts on the behavior of these storms and their potential to produce hazardous weather, including tornadoes. Additionally, growing up in the southeast and living in areas prone to natural hazards influenced my decision to learn and study more about these phenomena.

TABLE OF CONTENTS

LIST OF TABLES

LIST OF FIGURES

ABSTRACT

Rain drop size distributions (DSDs) in severe convective storms are highly variable in time and space. DSDs can be derived from polarimetric radar observations at high spatiotemporal resolution but these observations are often lacking near the surface owing to radar horizon issues. Disdrometers provide "ground-truth" measurements and validation of radar-derived DSDs but are by nature limited point measurements. Moreover, substantial evolution of the DSD can occur between the lowest radar elevation angle and the surface. Recent studies have shown that hydrometeor size sorting (HSS) is an important and even dominant process contributing to DSD evolution in severe storms; many physical processes such as the strength of the updraft, transient effects, and storm-relative mean winds are contributing factors to continued size sorting. In this study, we focus on strong storm-relative mean winds that induce sustained size sorting owing to the different residence times of hydrometeors of different sizes as they fall in severe storms. The resulting differential advection leads to a distinct horizontal spread of hydrometeors of different sizes at the bottom of a given layer. The goal of this study is to evaluate the impact of size sorting on DSD evolution from the radar level to the surface. To accomplish this, we develop and apply a raindrop trajectory model to compute the evolution of DSDs between radar observations aloft and the surface. For simplicity and to isolate the effects of size sorting, we neglect processes such as breakup, collection, and evaporation, and assume a horizontally homogeneous wind profile. We use disdrometer and radar data, which measure DSDs at the surface and provide the observed quantities aloft, respectively. The disdrometer data was collected from portable disdrometers as a collaboration between Purdue University, University of Oklahoma, University of Massachusetts, and the National Severe Storms Laboratory during the VORTEX-SE 2017 field campaign. NEXRAD data from KHTX Huntsville, AL and KGWX Columbus Air Force Base, MS was retrieved from the National Centers for Environmental Information (NCEI).

We evaluate three separate cases, a tornadic QLCS on 30 April 2017, a cluster storm on 27 March 2017, and a squall line on 25 March 2017. After the radar data is pre-processed, we retrieve the DSDs from the radar by assuming a gamma distribution and discretize them into PARSIVEL bins to produce a gridded dataset of DSDs. We then apply the raindrop trajectory model to compute the DSDs at the surface which are then compared directly with disdrometer observations. Analysis and comparisons from all cases yield similar results in that-the sorted radar DSDs at the surface

are overall closer to the disdrometer observations than the original radar DSDs aloft. Results also show that the spatial variation of DSDs is higher at the surface due to size sorting by the storm-relative mean winds.

1. INTRODUCTION

DSDs vary with height because of several processes, including collision, coalescence, evaporation, spontaneous breakup, and size sorting. Storm-relative winds can induce sustained size sorting owing to the different residence times of drops of different sizes as they fall toward the ground, resulting in variable horizontal advection leading to a distinct horizontal spread of drops of different sizes at a given height. Numerous recent studies based on scanning radar observations and numerical simulations have shown that this process can explain certain low-level microphysical features in convective storms. Rain DSDs can continue to evolve between the lowest radar elevation scan and the surface. Changes in DSD shape and mean diameter consistent with size sorting can therefore serve as a proxy to changes in the near-surface wind profile near storms. In tornado environments, the strongest shear and storm relative flow can exist below the radar. Quantifying this evolution can have some good benefits such as an improved understanding of how low-level storm dynamics and microphysics interact, improvements to radar-based precipitation algorithms, and nowcasts of storm structural changes leading to tornadogenesis. The goal of this study is to evaluate the impact of size sorting on DSD evolution from the radar level to the surface in southeast-U.S. convective storms by applying a simple trajectory model to radar-retrieved DSDs and comparing them directly with surface disdrometer observations. Typical radars don't provide good information close to the ground but are often the only source of microphysical information aloft. Retrieval of the DSD from radar observations is needed, since it only observes quantities related to bulk moments (for example, the reflectivity related to the 6th moment), while disdrometers directly measure the DSD.

The southeastern United States (Fig. 1a) experiences many severe storms annually. According to statistics from the US Department of Commerce, Alabama has two tornado seasons; one during the average spring season from March through May and the other during the fall around late November (www.weather.gov/bmx/tornadostats2). In part due to this, it has become a prime region for experimental studies. The Verification of the Origin of Tornadoes Experiment-Southeast (VORTEX-SE) is a research program to help understand how the environmental factors that are characteristic of the Southeastern U.S. affect the formation, intensity, structure, and path characteristics of tornadoes for this region (Rasmussen 2015). Many of the reported thunderstorms occur in the western region of the state and according to Ashley (2008) and Rasmussen (2015),

tornadoes in the southeast occur during the night much more frequently than other regions. The southeastern tornado environments differ in many ways from their better studied Great Plains counterparts. The region consists of more frequent cold-season (low-CAPE) environments, more frequent nocturnal tornadoes, and more tornadoes that develop in quasi-linear convective systems (QLCS) vs. supercell modes. These environmental differences influence storm microphysical processes and associated feedback to thermodynamic and dynamic processes related to tornadoes and other hazards in poorly understood ways. As a first step toward improving our understanding of these differences, it is important to better characterize important microphysical-dynamical interactions such as storm-relative wind-induced size sorting. The rich set of observations from the VORTEX-SE field program will help us do that. According to Ashley (2008), nocturnal tornadoes are a large factor in the rising death total in rural areas due to vulnerable housing structures, such as mobile homes, lack of visual evidence, inability to hear sirens at night while indoors and sleeping, or according to Rasmussen (2015) high false alarm rates (FAR) which are associated with low lead-time and missed events.

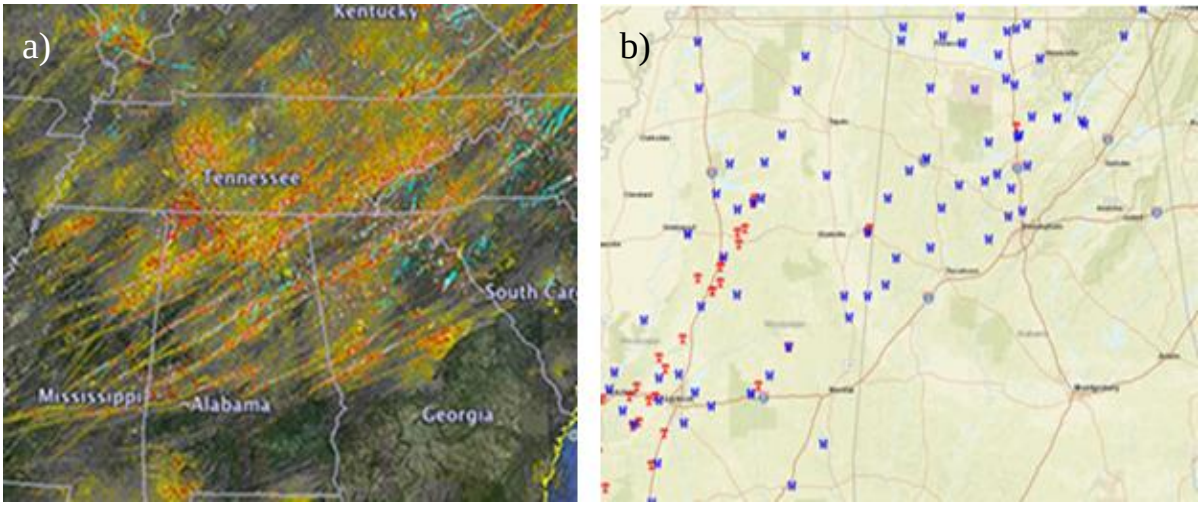

Figure 1. Rotation tracks (a) captured by NSSL's On-Demand system of the devastating tornadoes in the southeastern U.S. on April 27–28, 2011. Bright reds and yellows show more intense circulations (image adapted from www.nssl.noaa.gov/projects/vortexse/). (b) Storm reports for 04/30/2017 during VORTEX-SE through Mississippi and Alabama. Red "T" represents tornadoes; Blue "W" represents high winds (image adapted from www.spc.noaa.gov).

For this study, we utilized WSR-88D radars and portable in-situ precipitation stations (PIPS) that include PARSIVEL (PARticle SIze and VELocity) laser disdrometers (Löffler-Mang and Joss 2000, Friedrich et al. 2013), as well as instruments to measure relative humidity,

reflectivity, temperature, pressure, rain rate, wind speed, and direction. The four PIPS deployed during the VORTEX-SE field program were located at the Scottsboro Airport, Scottsboro, Alabama and various locations throughout the Lawrence County, Alabama area. We examine three convective storm events that passed over the sites on 25 March 2017, 27 March 2017, and 30 April 2017. The 25 March 2017 case featured a nontornadic squall line that moved over the PIPS site from southwest to northeast. It was the least intense of the three cases, but provided relevant data. The 27 March 2017 case featured a tornadic multicellular cluster thunderstorm whose individual cells passed over PIPS 1A at ~1945 UTC, PIPS 1B at ~2100 UTC, and PIPS 2B at ~2115 UTC, from northwest to southeast. The storm produced seven tornadoes over Mississippi, Tennessee, and Kentucky with no confirmed tornadoes reported in Alabama. Many hail and high winds were reported in northwest Alabama associated with embedded supercells. The 30 April 2017 case featured a weakening QLCS with embedded circulations. The QLCS advanced from southwest to northeast across the northern Alabama VORTEX-SE domain. The storm produced several tornadoes throughout Mississippi but weakened in tornadic activity as it approached west Alabama. Embedded circulations persisted with one confirmed tornado reported over central Alabama. According to NOAA/NWS Storm Prediction Center, the National Weather Service survey team found evidence of an EF-0 near Cullman, AL, around 1912 UTC just southwest of Huntsville, AL.

We will present results characterizing the vertical and temporal variation of DSDs in these events, compare with predictions of idealized models of size sorting owing to the storm-relative winds using near-storm wind profiles derived from observations and model analyses, and discuss differences between the cases.

2. BACKGROUND

2.1 Rain DSD Measurements

2.1.1. Historical Measuring Methods

Before the development of instruments used for measuring DSDs, there were other laborious and tedious ways to measure raindrop sizes. One method was the European style of using sheets of filter paper brushed with water-soluble dye and exposing it to rain for momentary periods (Laws and Parson 1943). Once the raindrops contacted the filter paper, they produced permanent spots. A drop size template is then created and used in conjunction with calibrated drops of a known volume for size comparison. Although this approach allowed for good observations of raindrop size, larger raindrops splattered on impact causing an increase in error. Another method was the flour method of size measurement. This method used a pan of one-inch, uncompacted, smooth surface flour in a tin receptacle (Laws and Parson 1943). After the raindrops fell in the flour, they absorbed the flour and formed dough pellets that hardened as they dried, corresponding very closely to the actual raindrop size.

2.1.2. Modern Measuring Instruments

Over the years, technological advancements in developing electronic disdrometers have made measuring drop sizes automatic and exponentially less tedious. Some popular DSD measuring devices are the impact disdrometer, two-dimensional (2D) video disdrometer, and PARSIVEL laser disdrometer (Joss and Waldvogel 1969) and (Kruger and Krajewski 2001). The impact disdrometer uses a sensor that is exposed to the rain allowing it to transform each impacted raindrop into an electrical pulse to interpret the diameter of each drop. It consists of two main parts; the sensor that receives the impacted raindrops via a conical styrofoam body and the processor that supplies power to the sensor, processes the signal, and tests the instruments performance. The 2D video disdrometer archives orthogonal image projections of raindrops to provide the raindrops size, shape, and velocity (Kruger and Krajewski 2001). It has three main components which consist of the sensor unit, the outdoor electronic unit (OEU), and another internal PC (Kruger and Krajewski 2001). The PARSIVEL laser disdrometer measures size and velocity of hydrometeors using a rectangular sheet of laser light. They can be stationary and when

deployed in pairs, they are often set up perpendicular to each other or articulating, designed by the University of Florida (Friedrich et al. 2013). As hydrometeors pass through the sampling area, it disrupts the light intensity between the transmitter and receiver. The duration and magnitude of the disruption is proportional to the particle velocity and size, respectively.

2.2 Fitting DSDs

Marshall and Palmer (1948) analyzed DSDs from summer rainfall in Ottawa, Canada and found that an exponential distribution provided a good fit to the data:

$$N(D) = N_0 \, exp \, (-\Lambda D) \, , \tag{1}$$

where *N(D)* (m^{-3} cm^{-1}) is the number of raindrops per unit volume per unit size interval having equivolume spherical diameter *D* (cm), with N_0(m^{-3} cm^{-1}) and Λ(cm^{-1}) as the intercept and slope parameters of the distribution, respectively.

For their dataset, Marshall and Palmer (1948) found that N_0 was a constant and Λ varies with the rainfall rate. Exponential distributions work well for DSDs that are averaged over long time periods; however, for shorter sampling periods, natural rain DSDs contain both fewer large and fewer small drops (Vivekanandan et al. 2004).

According to Ulbrich (1983), the suggested appropriate form to analyze DSDs uses the gamma distribution form,

$$N(D) = N_0 D^{\mu} \, exp \, exp \, (-\Lambda D) \, , \tag{2}$$

where the shape parameter μ can have any negative or positive value. The gamma distribution (2) thus has three free parameters; the exponential distribution (1) is the special case with μ = 0. Ulbrich (1983) introduced (2) owing to its greater flexibility and capability of describing a wider range of DSDs found in nature: “previous analyses imply that variations in the form or shape of DSDs occur commonly in nature and that DSD variations found between different rainfall types are similar to those found from moment to moment within a given rainfall type” (Ulbrich 1983). Using the three-parameter gamma distribution better characterizes instantaneous rain DSDs (Vivekanandan et al. 2004).

2.3 Storm Dynamics and Microphysical Process

To understand storm dynamics, we take into account the microphysics of clouds. Clouds form when air becomes supersaturated with respect to water or ice (Wallace and Hobbs 2009). Since the atmosphere contains many particles of many sizes, droplets can form on those particles if they are wettable. Those wettable particles form the cloud condensation nuclei (CCN) of the droplet. Clouds that form below (above) the 0°C isotherm are warm (cold) clouds and contain only water (ice particles and/or supercooled) droplets (Wallace and Hobbs 2009). In warm clouds, droplets grow by condensation and by colliding and coalescing with other droplets. Droplets that do not coalesce after a collision will break upon impact, follow a streamline around the collector drop, or simply bounce off one another. Condensation allows droplets to continue growing; the smaller the droplet the faster its growth rate. As droplets continue to increase in size, their terminal velocities increase, and growth by collision and coalescence becomes more likely.

Cloud prediction is beneficial for forecasting times and locations of severe weather, but may prove problematic and intricate to represent in models (Griffin et al. 2020). The dynamical structure of clouds and storms depends on the organization of convection from environmental conditions such as instability, lift, water vapor, and wind shear. Mechanisms that cause air parcels to lift can be due to fronts, jet streaks, vorticity, low level moisture advection, and low level convergence to name a few. An increase in moisture or water vapor in the lower troposphere coupled with dry air in the middle troposphere leads to an increase in storm severity. Since wind increases with height, strong vertical wind shear may lead to an increase in wind speed and/or wind direction further intensifying storms into a possible severe category. Once the warm moist air rises, they develop into single cell, multicellular clusters, multicellular lines, or supercell storms, depending on the magnitude and depth of the vertical wind shear.

Severe storms can produce a magnitude of meteorological phenomena that are amenable to observations and analysis. Severe storms must include at least one of the following conditions: wind greater than 58 mph (50 knots), hail one inch in diameter or greater, and/or a tornado (www.spc.noaa.gov/faq/#4.2). The fallout from thunderstorms may produce heavy rain, damaging winds, large hail, and tornadoes of all magnitudes (Klemp 1987). Microphysical processes affect the evolution of DSDs (Kumjian and Ryzhkov 2012) and DSDs are dominated by collection, evaporation, and breakup in convective storms (Freidrich et al. 2013). We care about these processes in severe convective storms due to the multitude of information it provides. Severe

storms can provide high precipitation, large sample regions for size sorting studies and a convective thunderstorm study conducted by Friedrich et al. (2013) revealed DSD changes rapidly in time and space.

2.4 Raindrop Size Sorting

HSS is an important process in severe storms. The physical processes that cause HSS include vertical wind shear, the strength of the updraft of a storm, an increase of terminal fall speed with diameter, and the storm relative wind field. "Updrafts and vertical wind shear can maintain size sorting, resulting in prolonged regions of particle size sorting" (Kumjian and Ryzhkov 2012) but as the updraft weakens or dissipates, smaller and larger raindrops fall with less of an opposing force acting on it. Many observations in convective storms have shown larger raindrops dominate the leading edge (defined with respect to the storm-relative flow) of the storm system owing to their steeper fall trajectories (Dawson et al. 2014) because they are heavier and their terminal fall velocity is faster than the updraft velocity. Smaller raindrops are constantly removed, lofted back up, and suspended in the storm until they collide and coalesce to form larger raindrops (or if lofted above the freezing level, they can freeze and become embryos for hailstones) therefore repeating the process. HSS associated with vertical wind shear has a longer lasting effect on smaller raindrops because they fall slower allowing them to be carried farther downstream by the storm-relative flow (Kumjian and Ryzhkov 2012).

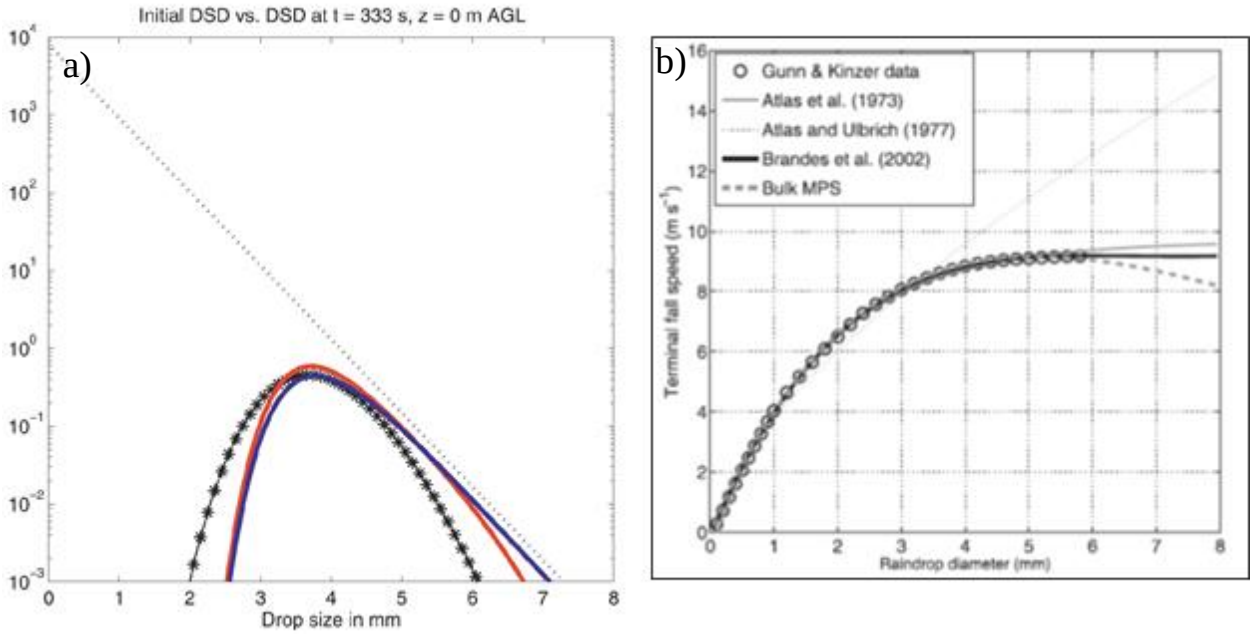

Figure 2 (a) shows size sorting results in narrowing of the DSD and increase in mean diameter near the storm-relative leading edge of the precipitation (Original Fig. 2(b) from Kumjian and Ryzhkov 2012). (b) Shows an evaluated raindrop terminal fall speed as a function of diameter. It shows the Brandes relation used in our study to specify the terminal velocity as a function of diameter (Original Fig. 1 from Kumjian and Ryzhkov 2012).

Dawson et al. (2015) found that nonzero storm-relative mean wind causes HSS, even in the absence of vertical wind shear. Based on the storm motion, the trajectories of larger raindrops impact the surface first, followed by medium drops, then smaller drops along the storm-relative mean wind vector. Severe storms evolve in environments with strong storm-relative winds that induce sustained size sorting owing to the different residence times of hydrometeors of different sizes as they fall. The resulting differential advection leads to a distinct horizontal spread of hydrometeors of different sizes at the bottom of a given layer. Dawson et al. (2014, 2015) showed that for a horizontally homogeneous wind profile, the gradient of Z_{DR} (a proxy of mean rain diameter) at the bottom of a precipitating layer is aligned with the direction of the storm-relative mean wind vector in that layer. This size sorting process manifests itself in distinctive low-level polarimetric radar signatures--particularly the "Z_{DR} arc"--in supercells (Kumjian and Ryzhkov 2009). QLCS's exhibit similar signatures (Mahale et al. 2012). This study focuses only on using storm-relative mean winds to analyze the size sorting effect and ignores contributions from updrafts and transient effects.

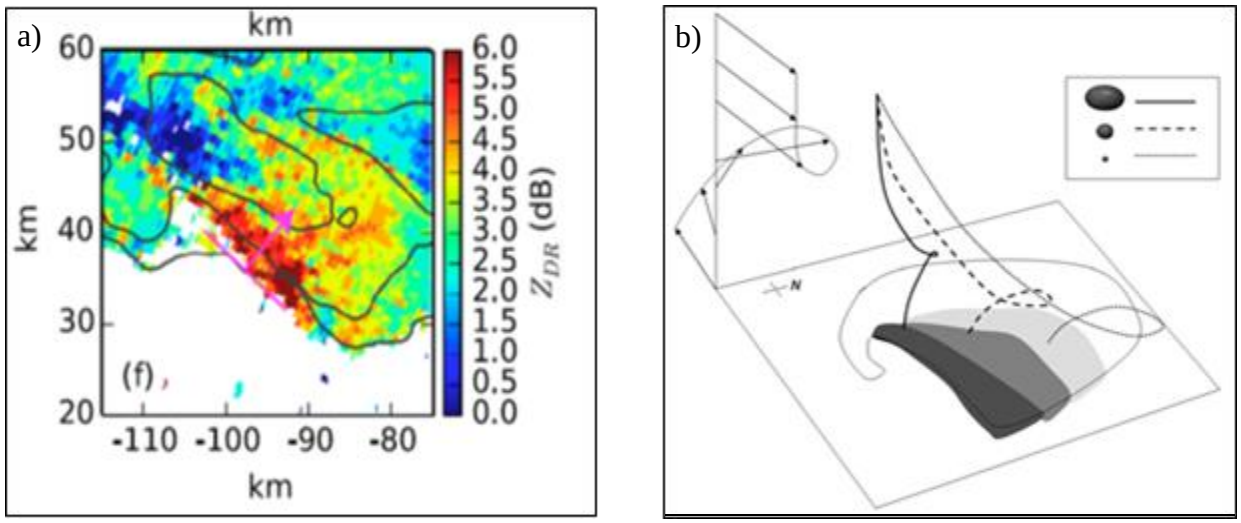

Figure 3. (a) Dawson et al. (2014, 2015) showed that for a horizontally homogeneous wind profile, the gradient of Z_{DR} (a proxy of mean rain diameter) at the bottom of a precipitating layer is aligned with the direction of the storm-relative mean wind vector in that layer (Original Fig. 3(f) in Dawson et al 2014). (b) Size-sorting process in distinctive low-level polarimetric radar signatures--particularly the "Z_{DR} arc"--in supercells. Shading represents the Z_{DR} enhancement, which is maximized at the leading edge (Original Fig. 2 in Kumjian and Ryzhkov 2009).

2.4.1. Impact of Size-sorting on Polarimetric Radar Variables

Size sorting can have impacts on polarimetric variables such as differential reflectivity, (Z_{DR}), horizontal polarization (Z_H), specific differential phase (K_{DP}), and cross-polar correlation coefficient (ρ_{hv}). Z_{DR} is the difference between the co-polar horizontal and the co-polar vertical reflectivity. High Z_{DR} is indicative of areas of larger raindrops since it is sensitive to the axis ratio (horizontal-to-vertical dimensions) of raindrops, and larger raindrops are increasingly oblate. When rain regions have a higher quantity of larger raindrops with a relative lack of smaller raindrops, Z_{DR} increases with increasing Z_H because the oblateness of the bigger raindrops increases them both (Kumjian and Ryzhkov 2012). Many models have shown that larger drops dominate the forward edge of precipitation regions (Gunn and Marshall 1955) although this is not always the case since observations have shown larger drops arriving after smaller drops, depending on the relative orientation of the storm-relative wind and storm motion vectors (Battan 1977, Dawson 2015). Sensitive to areas of heavy liquid precipitation, K_{DP} highlights these regions better than reflectivity alone.

3. DATA

3.1 Disdrometer Data

3.1.1. Data Collection

For this study, multiple PIPS were deployed throughout various locations in Alabama during the 2017 VORTEX-SE field program to collect DSD data in convective storms. PIPS 2A was located southeast of Huntsville, AL (lat: 34.6871 deg, lon: -86.0049 deg) and collected nearly continuous data from 03/24/17 16:58:07 to 05/01/17 15:31:43 UTC (Dawson et al. 2017). PIPS 1A, PIPS 1B, and PIPS 2B were deployed in northwest Alabama in various locations depending on the event. Table 1 and 2 describes details of their deployments in Intensive Operating Periods (IOPs) 1A and 1B of VORTEX-SE 2017 that are analyzed in this study. PIPS data was retrieved from the VORTEX-SE Earth Observing Laboratory (EOL) (https://data.eol.ucar.edu/dataset/541.029). The PIPS (Fig. 4) are small, portable instrumented platforms equipped with several meteorological instruments. These include a suite of sensors to measure temperature, relative humidity, wind speed and direction, and pressure. A GPS and a digital compass respectively allow for easy determination of location and of wind direction for arbitrary orientations of the probe. Finally, each PIPS is equipped with an OTT PARSIVEL^2 laser disdrometer that measures the size and number of objects that fall through the laser beam.

The optical sensor laser diode has a wavelength of 780 nm, output power of 0.5 mW, and a beam size of 180 x 30 mm^2. The PARSIVEL disdrometer works when particles pass through the laser beam disrupting the signal therefore decreasing the voltage. The instrument categorizes particles that fall through the sensing area into a 32 x 32 velocity/diameter count matrix (Dawson et al. 2017). The duration of the signal reduction and amplitude of the signal deviation allows for an estimate of particle velocity and is a measure of particle size, respectively (Löffler-Mang and Joss 2000). The DSD is measured at 10-s intervals and all other observations at 1-s intervals. The nominal measuring range of liquid precipitation is 0.2 to 5 mm (but can measure larger drop sizes that fall through the beam) and solid precipitation from 0.2 to 25 mm with the particle velocity ranging from 0.2 to 20 m/s (Tokay et al. 2013). The rain rate minimum to maximum intensity ranges from 0.001 mm/h (drizzle) to 1200 mm/h with an accuracy of +/- 5% for liquid and +/- 20% for solid. A micro-SD card located inside the datalogger housing records all data.

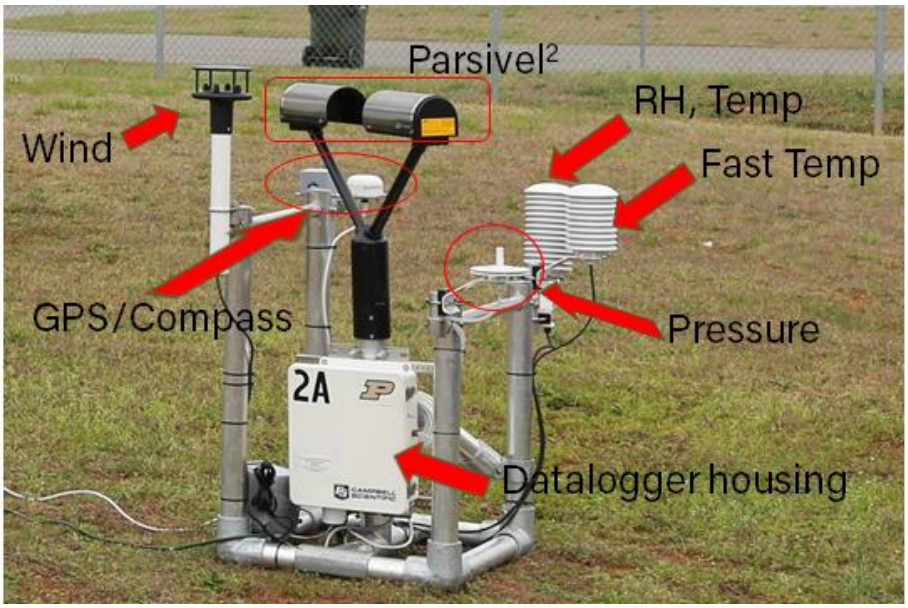

Figure 4. A photograph of PIPS 2A, with disdrometer and weather sensors labeled. (Image courtesy of Dawson, D. T.)

Table 1. PIPS deployment details for IOP1A during VORTEX-SE (Dawson 2020).

PIPS ID	**Date**	**Start time (UTC)**	**End Time (UTC)**	**Lat(deg)**	**Lon(deg)**	**Elevation (m ASL)**
PIPS 1A	03/25/17	17:28:30	18:45:45	34.5207	-87.2945	205
PIPS 1B	03/25/17	17:38:30	18:36:30	34.5587	-87.3373	215
PIPS 2B	03/25/17	17:47:50	18:25:00	34.5728	-87.3925	207

Table 2. PIPS deployment details for IOP1B during VORTEX-SE (Dawson 2020).

PIPS ID	**Date**	**Start time (UTC)**	**End Time (UTC)**	**Lat(deg)**	**Lon(deg)**	**Elevation (m ASL)**
PIPS 1A (D1)	03/27/17	19:48:20	23:18:17	34.8382	-87.3912	193
PIPS 1B (D1)	03/27/17	20:54:10	21:51:57	34.5587	-87.3373	217
PIPS 2B (D1)	03/27/17	21:02:00	21:42:09	34.5163	-87.2927	205

One advantage of the PARSIVEL^2 disdrometer (PD) is its low cost and lightweight, compared to other instruments, making it rapidly deployable. Its base is heavier and sturdy, preventing it from easily tipping during high winds. PDs use dwell times within its single beam and give the maximum dimension of the drop in only one plane (Thurai et al. 2011). However, overestimations tend to occur in PD DSDs with drops larger than 2.4 mm in diameter (Tokay et al. 2013). PDs also have a higher mean mass and rain rate, particularly at rain rates above 30 mm/h, compared to 2D Video Disdrometers, but with D_m< 2 mm and/or R< 20 mm/h they perform similarly (Thurai et al. 2011; Tokay et al. 2013). Possible causes of the overestimation may be due to the presence of graupel or hail during periods of higher rain rates as well as non-fully melted hydrometeors together with drop shape and velocity assumptions made by the PD for large drops (Thurai et al. 2011).

3.1.2. Data Filtering

For quality control, this study follows the filtering procedures of Friedrich et al. (2013) to remove unwanted particles from the sample area (Fig. 5). Strong winds, margin fallers, and splashing from particles lead to misclassification, errors, and unrealistic fall velocities and diameters. According to Friedrich et al. (2013), stationary (PIPS used in this study) and articulating disdrometers are prone to misclassification of particles with larger number concentrations of raindrops >5 mm in diameter and fall velocities <1-2 m/s. Articulating disdrometers observe higher concentrations of larger raindrops and higher concentration of medium sized raindrops compared to stationary disdrometers (Friedrich et al. 2013). Diameters >5 mm with velocities <1 m/s were removed to address this error. Margin fallers occur when raindrops fall through the edge of the laser beam, displaying as smaller drops with faster fall velocities, creating errors in the sampling area. Splashing errors occur when raindrops impact the disdrometer surface, break up, and fall through the laser beam, resulting in a wide variety of fall speeds and smaller drop diameters in the sampling area. These errors are filtered by removing particles that have fall velocities 60% above or below the fall velocity-diameter relationship for rain and that have a diameter <2 mm for splashing and <8 mm for margin fallers (Friedrich et al. 2013). In addition to the above QC procedures, this study removes all particles that are likely not rain, based on the classification scheme of Friedrich et al. (2013), as illustrated in Fig. 5. Raindrops should have diameters of < 8

mm (Rauber et al. 1991); any diameters larger are discarded and any remaining graupel and hail is removed.

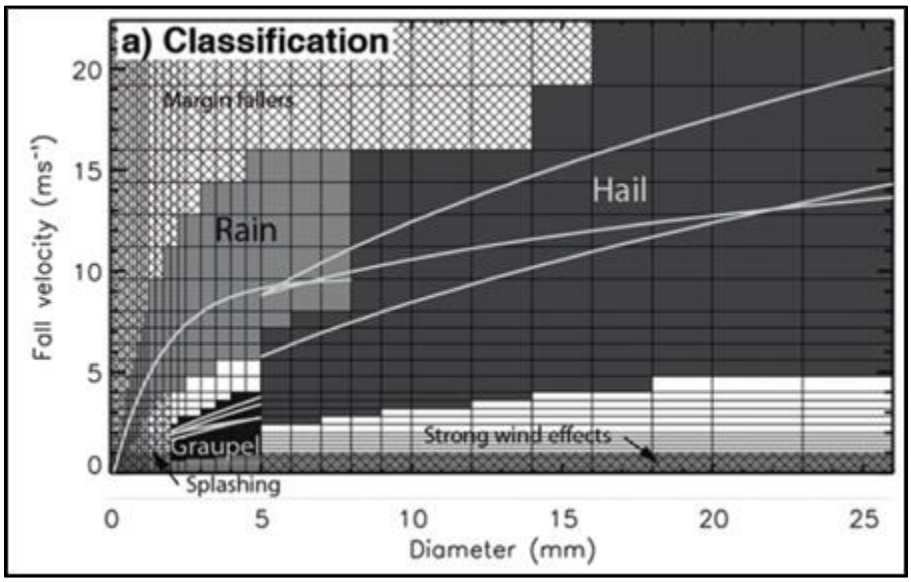

Figure 5. Particle hydrometeor classification scheme used to separate raindrops from other particles, based on fall velocity-diameter relationship. Light gray lines indicate rain, graupel, and hail respectively (Originally Fig. 5(a) in Friedrich et al. 2013).

3.2 Radar Data

For comparison, either data collection from the S-Band radar KHTX (Huntsville, AL) or the KGWX (Columbus Air Force Base, MS) WSR-88D is used due to its close proximity to the PIPS location during their deployments (www.ncdc.noaa.gov/nexradinv/). Radar beams increase in height farther away from the radar causing the variables they measure to change in response to changes in the DSD beneath the radar beam and surface. The distance between the PIPS location and the KGWX radar used for the 25 March 2017 and 27 March 2017 cases ranged up to ten times the distance between PIPS 2A and the KHTX radar used for the 30 April 2017 case meaning less DSD change occurred in the 30 April 2017 case.

WSR-88D radars scan in clear air mode, completing 5 different elevation angle scans in 10 minutes and precipitation mode, completing 14 different elevation scans in 5-6 minutes. For the purposes of the analyses in this study, radar observations on the original elevation surfaces were remapped onto a regular grid with 1-km horizontal resolution and 100-m vertical resolution between 500 m and 10 km AGL.

Radar reflectivity, also known as echo intensity, is measured in decibels (dBZ) and represents the amount of transmitted radar energy returned to the receiver after hitting bugs, debris, birds, or in this case, precipitation (www.wunderground.com/prepare/understanding-radar). Decibel values range higher when the radar operates in precipitation mode vice clear air mode. A higher return signal at the radar leads to a higher dBZ value, which indicates greater rainfall rates. Reflectivity is a function of the underlying size distribution of precipitation particles. Since PARSIVEL disdrometers measure the DSD directly, the corresponding radar reflectivity can be calculated from the distribution. Under the Rayleigh approximation, the reflectivity (Z) is calculated from DSDs using

$$z = \Sigma_i D_i^6 / V \tag{3}$$

where z is proportional to the sixth power of the diameter of the i^{th} drop $D_i(\text{mm}^6)$ and a parameter that relates quantities measured by the radar to the DSD in a volume $V(\text{m}^{-3})$. From there, we can express the linear reflectivity factor in a logarithmic scale,

$$Z = 10 \log_{10}(z) \tag{4}$$

measuring Z in decibels (Rauber and Nesbitt 2018). Our approach, however, makes use of a polarimetric radar simulator (Jung et al. 2010, Dawson et al. 2014) based on the T-matrix method (Watermann 1969) to compute not only the radar reflectivity but several polarimetric observables as well, including Z_{DR}, K_{DP}, and ρ_{hv}. Equations (3) and (4) nevertheless provide an excellent approximation to Z for rain for the S-band radars used in this study.

4. METHODOLOGY

4.1 Overview

Analyses of radar observations in this study were confined to levels below the melting layer to minimize the impact of frozen precipitation, which can contaminate or cause more errors in the sample. Particularly in tornado environments, strong shear and storm-relative flow can exist in the lowest few hundred meters AGL (e.g. Esterheld and Giuliano 2008, Coffer et al. 2019). To quantify the evolution, a simple raindrop trajectory model applied to DSDs retrieved from radar observations of severe storms and compared with disdrometer measurements is applied. Disdrometer observations provide "ground-truth" measurements of DSDs compared with radar-based DSD retrievals aloft. The trajectory model assumes the vertical profile of the horizontal wind is horizontally homogeneous and that vertical air motion is zero everywhere. Other assumptions and approximations are made for simplicity and to isolate the effect of size sorting. Specifically, we assume that there are no interactions between drops, no breakup, and no evaporation. Assuming no breakup may yield too many large drops and assuming no evaporation or condensational growth may mean that more smaller drops make it to the surface than actually would. Also, neglecting collision and coalescence means that their overall broadening effect on the distribution is not considered. All drops fall at a diameter-dependent empirically defined terminal velocity (Brandes et al. 2002; Fig. 2b), and the effect of changing air density on terminal velocity is neglected.

4.2 Radar Data Pre-processing

Python ARM Radar Toolkit (Py-ART) provides the framework for working with radar data and is used to visualize, correct, and analyze radar data from weather radars in Python (Helmus and Collis 2016). Py-ART was used to bring the NEXRAD Level-2 radar to regular 1 km grids. A 1 km height is extracted from the gridded radar dataset and used for the 04/30/2017, vice a 2 km height used for the 03/25/2017 and 03/27/2017 case. We applied an optical flow advection-correction method using pysteps, developed by Pulkkinen et al. (2019), to interpolate the storm evolution between the original 4-5 minute radar scan times to 1-min intervals. This method yields a flow field that represents the local advective velocity of the reflectivity pattern (Fig. 6). From

this, we derive the storm motion vectors that are plotted on the various hodographs in section 5 for each case.

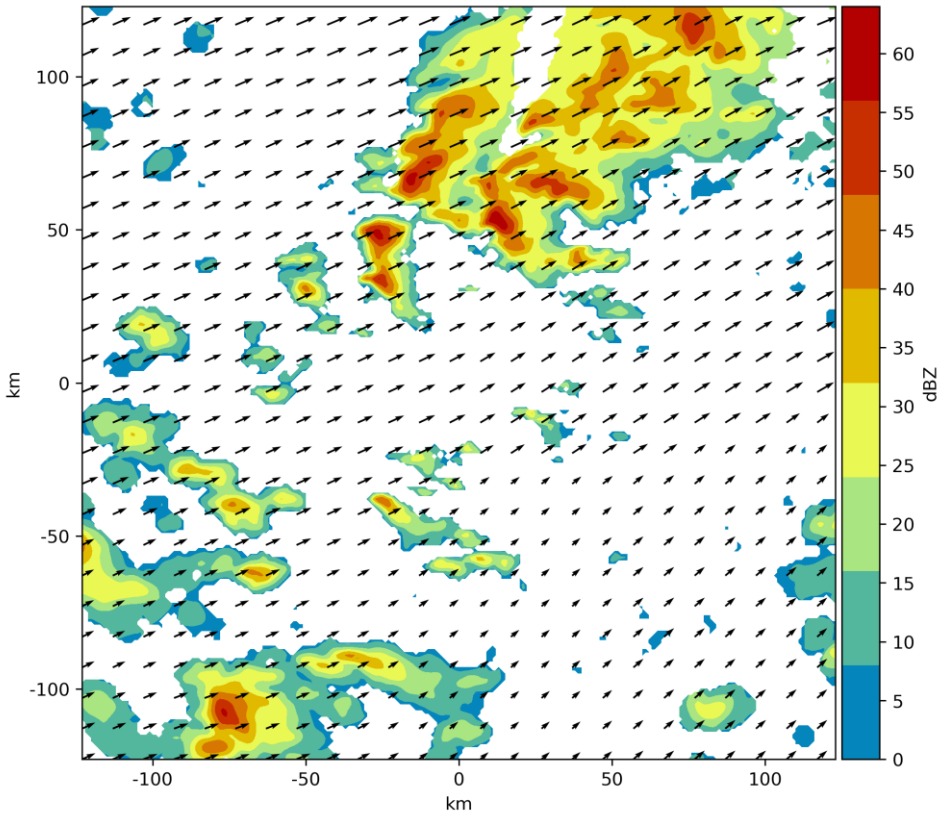

Figure 6. Advection correction with pysteps of the 03/27/2017 case. The flow field (black arrows) represents the local advective velocity of the reflectivity pattern (color fill).

4.3 DSD Retrieval from Radar and Gridding

It is important to use an appropriate set of moments when estimating DSD parameters. Many researchers have used various combinations of moments to estimate DSD parameters with the method of moments, or an estimation method of choice. DSDs are assumed to be a gamma distribution (Eq. 2) and we retrieve its three parameters N_0, λ, and μ from the radar parameters reflectivity (Z) and differential reflectivity (Z_{DR}), which depend mainly on the raindrop shape and size (Zhang et al. 2001). Ulrich (1983) suggested using the gamma distribution for illustrating a raindrop spectra and Smith et al. (2005) proposed using M234 because they gave the least error for the estimate of DSD parameters for DSDs that follow a gamma distribution fit. According to Zhang et al. (2001), Ulrich used a N_0- μ relation but it was too noisy for their study which led to

deriving disdrometer observations from a constrained μ-Λ relation. “It is possible that the μ-Λ relationship changes depending on climatology and rain type” (Zhang et al. 2003). Polarimetric radar measurements and radar reflectivity have allowed alterations to the μ-Λ relation. Statistical uncertainties can be attributed to errors between the μ and Λ parameters (Moisseev and Chandrasekar 2007). Zhang et al. (2001) suggested N_0, λ, and μ can be solved from any three moments but in their study, the second, fourth, and sixth moments fit the measurements well and give consistent rain rate estimations. Following this method, we retrieve the DSDs from the radar by assuming a gamma distribution and discretize them into PARSIVEL bins to produce a gridded dataset of DSDs (Fig. 7). The different colored curves are different exponential and gamma distribution fits using the method of moments and the sorting and averaging of two parameters (SATP) method (Cao et al. (2008). The transition (T) matrix method (Watermann 1969 and Vivekanandan et al. 1991) is used to look up scattering amplitudes and phases.

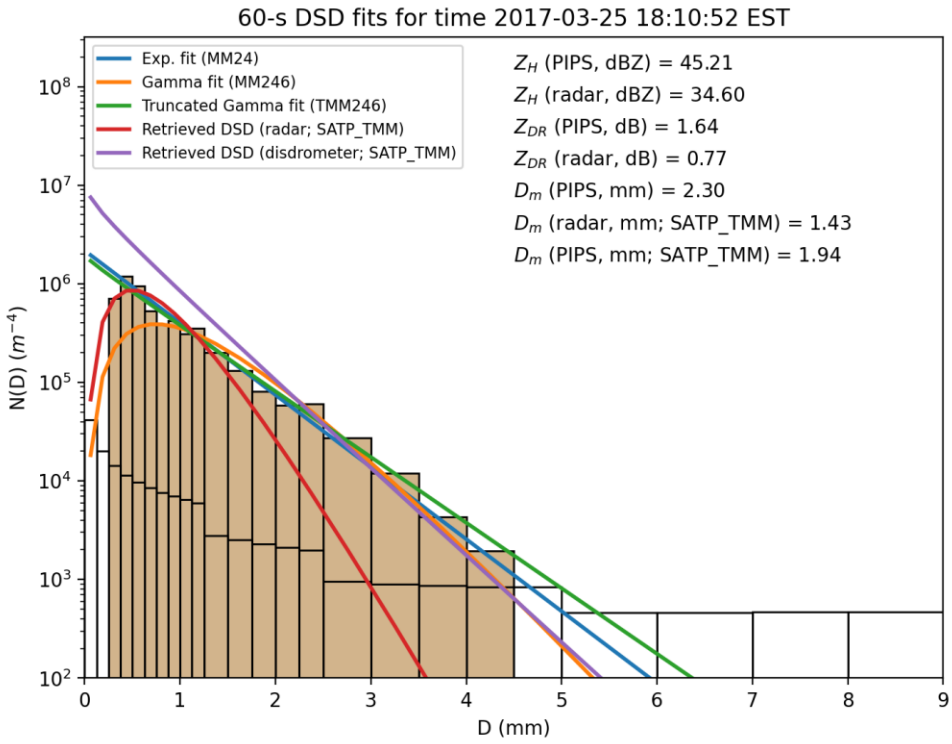

Figure 7. 60-s PARSIVEL DSD (tan histogram) and several for ~18:11 UTC 03/25/2017. The white transparent histogram is the DSD for the case of only one drop per bin. After Zhang et al. (2001) and Cao et al. (2008), several exponential and gamma fits using the method of moments (MM), truncated method of moments (TMM), and sorting and averaging of two parameters (SATP) as applied to the observed and overlying radar observations are shown for reference.

Analyses were performed using a series of Jupyter notebooks (Kluyver et al. 2016). The original NEXRAD Level-2 files for each case were mapped to a regular 1-km grid using py-ART (Helmus and Collis 2016). Pysteps was used to temporally interpolate the radar observations to 1-min intervals using an optical flow method.

Gamma DSD parameters (λ, N_0, and μ) were retrieved from Z and Z_{DR} using the method of moments and the constrained-gamma method of Zhang et al. (2001). The final set of gridded radar variables interpolated to 1-min intervals was then saved to disk for each case in preparation for the application of the trajectory model.

4.4 Trajectory Model

We apply a simple raindrop trajectory model to disdrometer and radar observations of severe storms. Low level wind profiles are ingested from proximity soundings for each case. Multiple trajectories for each size bin, grid point, and time are initialized at a given radar grid level aloft. Endpoints of trajectories at the surface are solved analytically knowing the terminal velocity and mean wind in the layer (Dawson et al. 2015). The trajectory endpoints of raindrops form a line oriented along the storm-relative mean wind direction in the layer and their horizontal spread can quantify the amount of size sorting in that layer (Dawson et al. 2015). Smaller drops fall further away from the initial points (Fig. 8). We choose the 1 km AGL for the 04/30 case and a 2 km AGL for the 03/25 and 03/27 cases then refine the horizontal grid from 1 km to 250 m to initialize the trajectories. We allow them to fall from all grid points at the top of the layer and hit the surface. We then re-bin the collection of trajectory endpoints into a new horizontal grid at the bottom which provides the final set of gridded DSDs at the surface. This procedure is described in more detail in the next two sections.

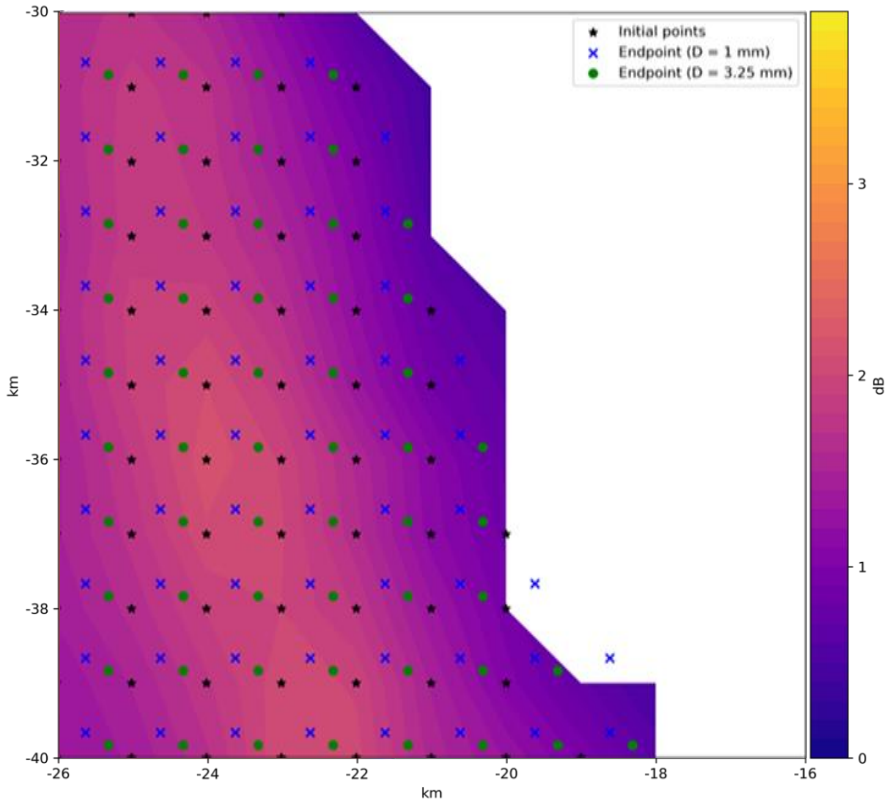

Figure 8. Example Z_{DR} field (color fill) overlaid with trajectory endpoints of a quantity derived from the original retrieved DSDs at 1 km AGL for the 04/30/2017 case.

More specifically, ND was calculated for each grid point from gamma distribution parameters using PARSIVEL bins. Next, the precipitation trajectory grid was set up for height above ground level (1 km for the 04/30 case and 2 km for the 03/25 and 03/27 cases), interpolated sounding for *u* and *v*, storm-relative winds, and layer-mean storm-relative winds. The diameter range was truncated for less than 9 mm and the range of terminal velocities were computed from Brandes relation. Three dimensional bins (two for space and one for time) were set up for the bottom of the sorting layer and 3D histograms (x, y, t) were created for number density for each diameter bin for drop trajectory endpoints.

4.5 Computing of Final Surface DSDs

The final step is to recompute the DSDs at 1-min intervals as if we are measuring them with a disdrometer again at the surface. Surface trajectory endpoints are binned in time and space, weighted by the number density of each size bin followed by constructing new 1-min DSDs.

Derive DSD moment-related quantities and polarimetric observables give us the sorting model surface DSD.

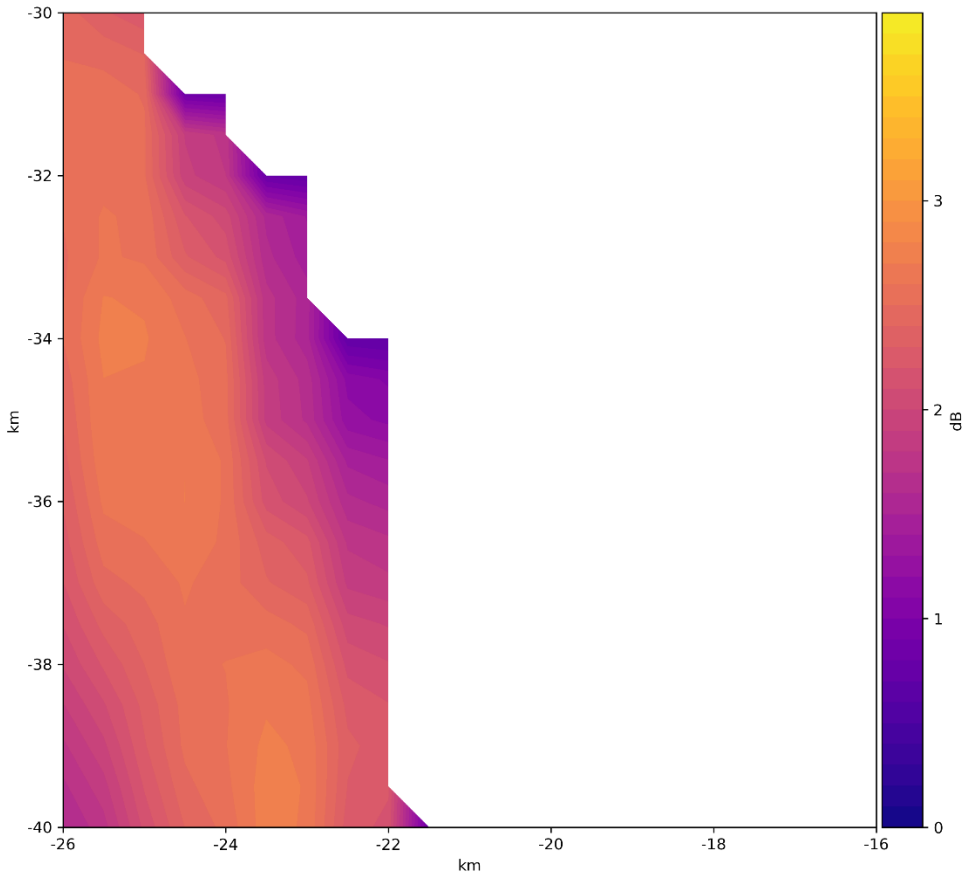

Figure 9. Example Z_{DR} field (color fill) derived from the sorted surface DSDs for the 04/30/2017 case.

4.6 Analysis and Comparison of Disdrometer and Final Sorted Radar DSDs

Large drops dominate radar parameters and radars poorly capture drops close to the surface (Friedrich et al. 2013). Disdrometers only receive a fraction of raindrops at the surface as compared to the large sample size of radars. PIPS locations are retrieved followed by calculating radar variables for new surfaces DSDs, plotting the Z and Z_{DR} at the bottom of the sorting layer, and Z and Z_{DR}1 km above ground level. The radar data at the PIPS location in conjunction with the filtered Z and Z_{DR} were plotted for each start and end time. Polarimetric fields are computed from PIPS DSDs then Z and Z_{DR} are interpolated from sorted grids to PIPS location. Afterwards, plots were created to show the comparison between the size sorting model, gridded reflectivity at the

top of the sorting layer, original raw radar data from the gates, and the observed surface DSD derived from the PIPS.

5. RESULTS

5.1 Case Studies

5.1.1. 04/30/2017

During the afternoon of April 30, 2017, a tornadic QLCS moved from southwest to northeast across the northern Alabama VORTEX-SE domain. We focus on the QLCS as it passed over the site of PIPS 2A, which was collocated with the UMASS FMCW profiling radar at Scottsboro Airport, Scottsboro, AL. The convective region of the QLCS passed over PIPS 2A from ~2040 to ~2115 UTC followed by a period of stratiform precipitation until ~0000 UTC on 1 May. A few shear vortices appeared on radar with tornado warnings in the Scottsboro area with no observed tornadic activity. The SPC reported one wind report for the county at 2055 UTC. Figure 10 shows the (left) reflectivity and (right) differential reflectivity as the QLCS passed over PIPS 2A location at 2040 UTC. It produced several tornadoes earlier in the day over Mississippi but weakened as it approached Alabama. Embedded circulations persisted, but only a single tornado report was received over central Alabama. The closest WSR-88D radar was the Huntsville, AL KHTX, which was located approximately 20 km northwest at a 640 m elevation scan.

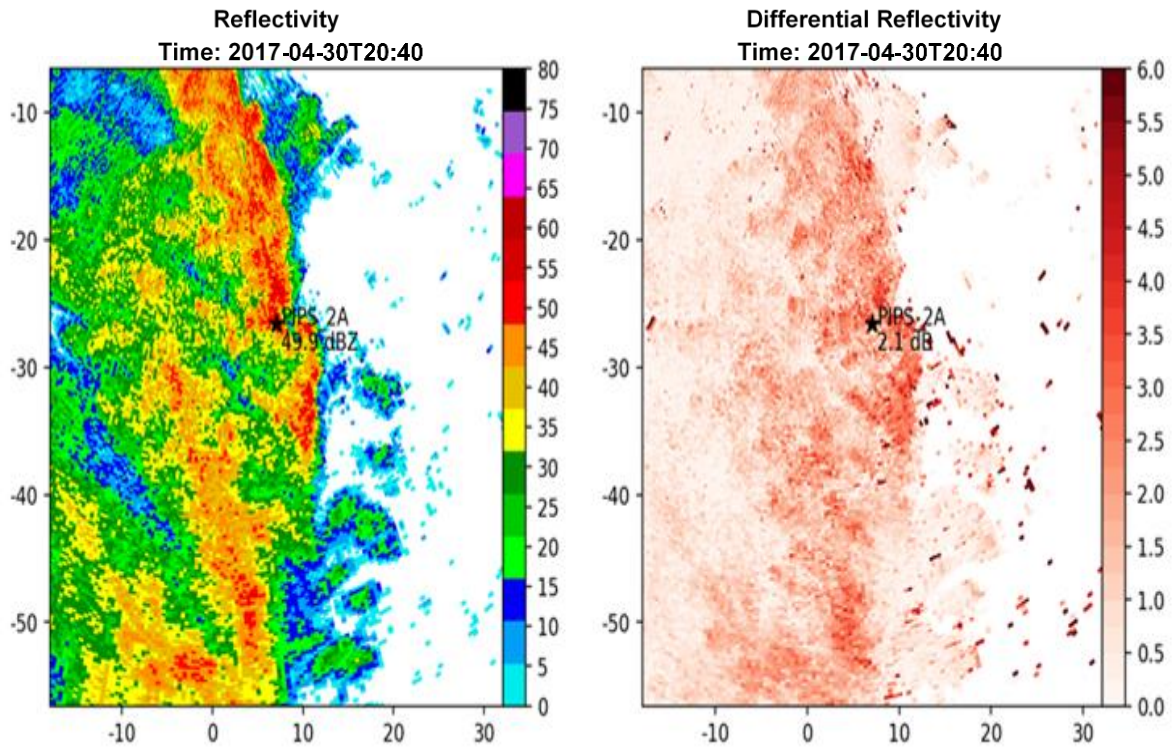

Figure 10. An overview of (left) reflectivity at 49.9 dBZ and (right) differential reflectivity at 2.1 dB at time 2040 UTC as the leading edge of the storm passed over PIPS 2A. Higher Z_{DR} at the leading edge representing larger raindrops, which can be a result of size sorting.

Figure 11 is a time series of the disdrometer-derived, radar-observed, and mass-weighted mean diameter of (a) Z and (b) Z_{DR} over PIPS 2A. The time series shows DSDs and associated quantities plotted at 1-min intervals with raindrop diameters plotted on the y-axis ranging from 0-9 mm and the number of concentration of drops using a color scale with a logarithmic range. A maximum reflectivity (~52 dBZ) and differential reflectivity (3.5 dB) were observed as the strongest convective region passed over PIPS 2A between 2040 and 2100 UTC. Both Z and Z_{DR} decreased as the storm entered its stratiform region after 2130 UTC, remaining below 36 dBZ and 1.5 dB, respectively. The radar reflectivity plotted in these figures is the ungridded reflectivity taken from the gate just above the disdrometer location. Overall, the Z and $Z_{DR}$of the PIPS vs. radar agree well throughout the entirety of the storm.

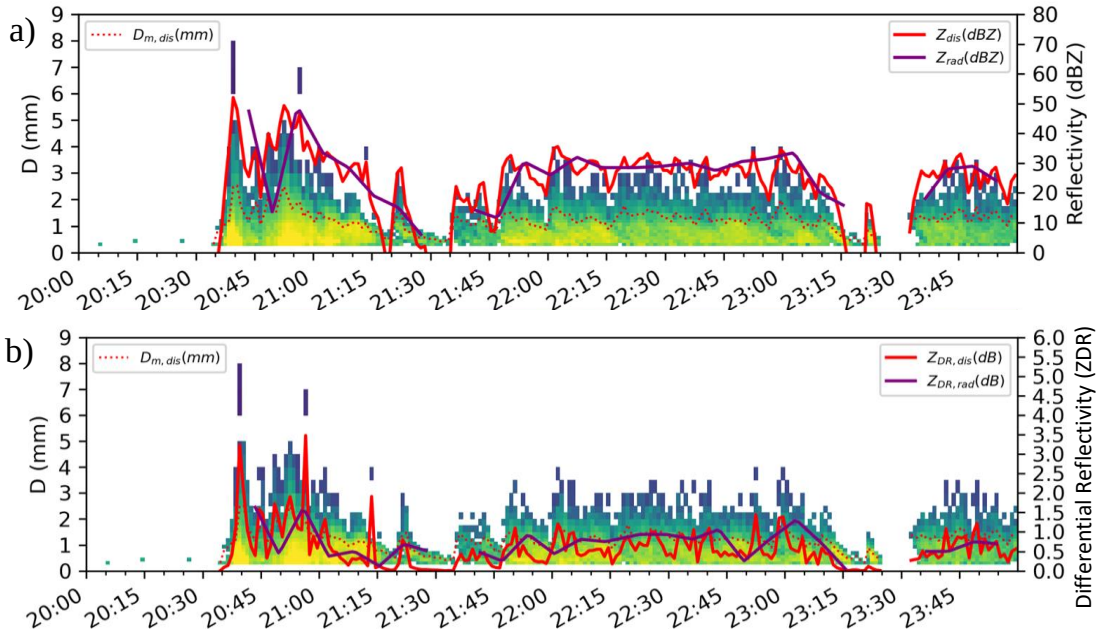

Figure 11. Time series of DSDs (color shading is number density) from PIPS 2A on 04/30/2017 of (a) reflectivity and (b) differential reflectivity. Red, purple, and red-dotted lines denote disdrometer-derived, radar-observed, and mass-weighted mean diameter, respectively.

Surface DSDs obtained from binning the drop trajectory endpoints are used to compute quantities such as radar reflectivity. Gridded reflectivity at the surface, after applying the precipitation trajectory model, tends to be somewhat higher than the gridded radar reflectivity at the top of the sorting layer (probably due to neglecting break up in the models). A 0-1 km AGL sorting layer was used for this case. Differential reflectivity at the surface exhibits an enhancement at the leading edge of the QLCS. This enhancement at the surface relative to that at 1 km AGL is consistent with size sorting by the easterly storm-relative mean wind in the 0-1 km layer as shown by the hodograph (Fig. 14). This hodograph is derived from a special VORTEX-SE sounding taken at 1954 UTC near Hollywood, AL and is representative of the inflow environment of the QLCS and strong wind shear with height. The distribution shifts towards larger drops near the leading edge because the smaller drops are advected farther downwind relative to the large drops, resulting in a horizontal redistribution of raindrops by size. The Z_{DR} gradient is stronger at the surface compared to 1 km because of the sorting over this layer.

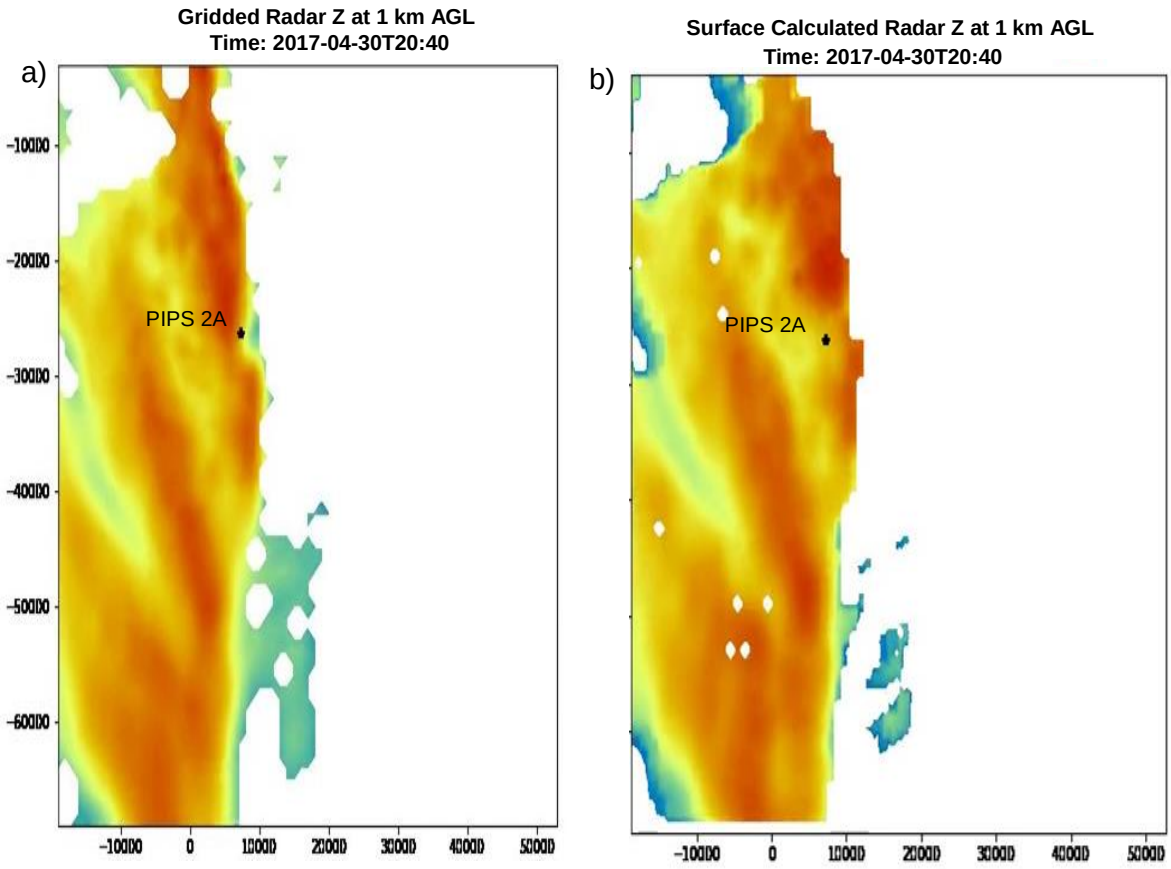

Figure 12 (a) gridded radar reflectivity at the top of the layer (1 km AGL) and (b) gridded reflectivity at the surface after applying the precipitation trajectory model. Surface calculated reflectivity shows a higher enhancement at the leading edge.

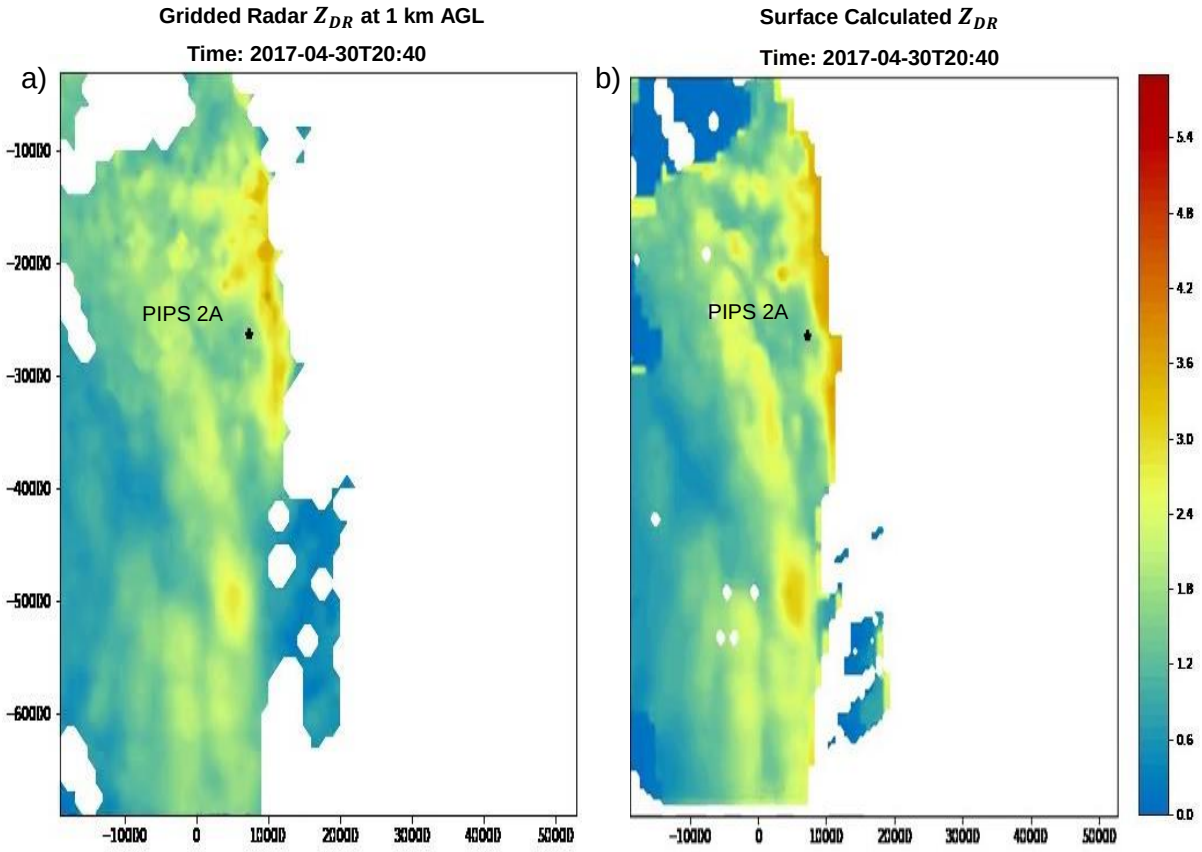

Figure 13 (a) and (b) are the same as Figure 12 (a) and (b) but with differential reflectivity. Enhancement at the surface relative to that at 1 km is consistent with size sorting by the easterly storm-relative mean winds in the 0-1 km layer.

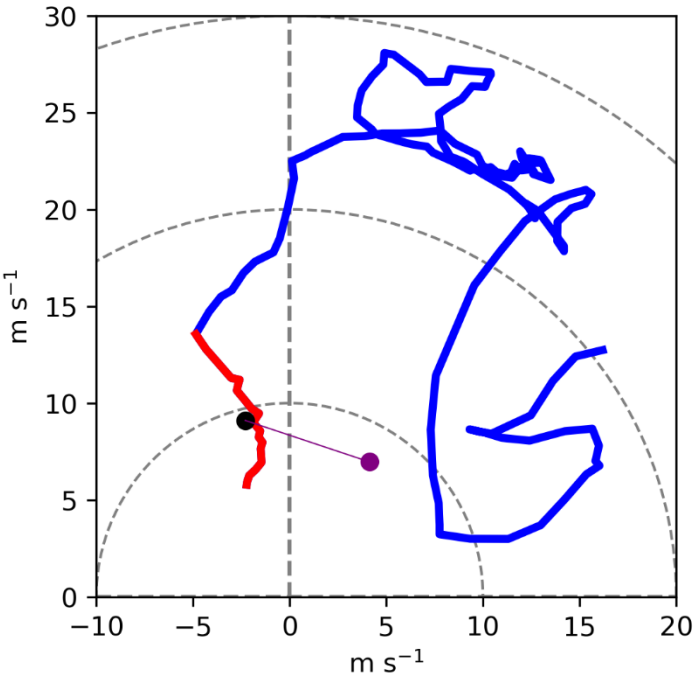

Figure 14. Hollywood, Alabama 1954 UTC special VORTEX-SE sounding hodograph. The 0-1 km layer is in red, above 1 km layer in blue, the black dot represents the mean winds between the surface and 1 km, purple dot is the storm motion, and the purple line is the 0-1 km storm-relative mean wind vector.

Finally, a time series of Z and Z_{DR} is shown in Figure 15. Z and Z_{DR} at PIPS 2A from the trajectory model are in better agreement with the disdrometer than the original radar at 1 km AGL. This is particularly true regarding the timing and magnitude of Z and Z_{DR} at the leading edge. The position of the peaks for Z and Z_{DR} shows that the surface DSD produced from the sorting model is in better agreement with the observed surface DSD at PIPS 2A. Particularly looking at Z_{DR}, the magnitude at the leading edge for the sorting model surface DSD is in better agreement with the surface PIPS observation.

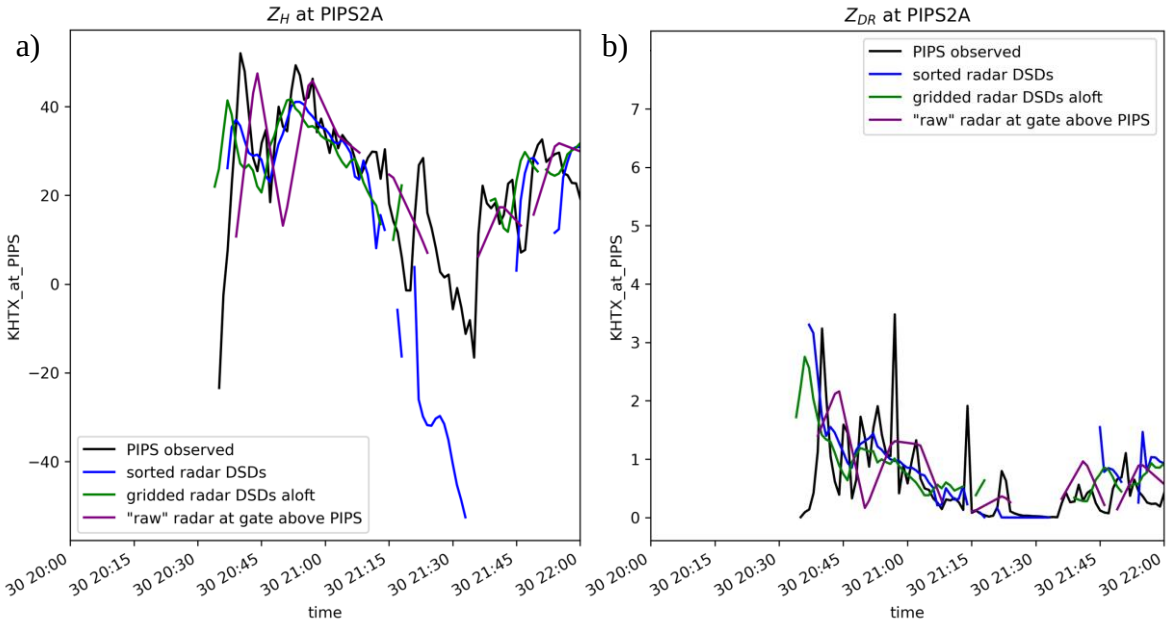

Figure 15. A time series of (a) reflectivity at PIPS and (b) differential reflectivity at PIPS. Black line indicates the derived reflectivity and differential reflectivity from the PIPS observation, red line is the 1 km AGL radar observation, and the blue line is the sorting-model surface DSD after sorting the trajectory model and extrapolating it to the surface.

5.1.2. 03/27/2017 IOP 1B-D1

On the afternoon of March 27, 2017, a cluster of occasionally tornadic storms passed over PIPS 1A, PIPS 1B, and PIPS 2B from northwest to southeast, respectively. The cluster produced several tornadoes over Kentucky, Tennessee, and Mississippi before weakening as it approached the PIPS locations in northwest Alabama. The cluster began dissipating as it moved farther southeast, but PIPS 1B encountered the strongest cluster. There were several hail and high wind reports from the cluster over Alabama, but no confirmed tornadoes. PIPS 1A was located north of the Tennessee River (just north of Lawrence County, AL), PIPS 1B and PIPS 2B were located in southeast Lawrence County, AL and the closest WSR-88D radar was Columbus AFB, MS KGWX, which was located ~209 km southwest of PIPS 1A, ~188 km southwest of PIPS 1B, and ~193 km southwest of PIPS 2B. The mean height of the radar beam over PIPS 1A, PIPS 1B, and PIPS 2B is 2323 m, 1851 m, 1881 m, respectively. Figure 16 shows (a) KGWX radar reflectivity imagery of the storm as it approached the PIPS locations and (b) the tornado, wind, and hail reports from the Storm Prediction Center.

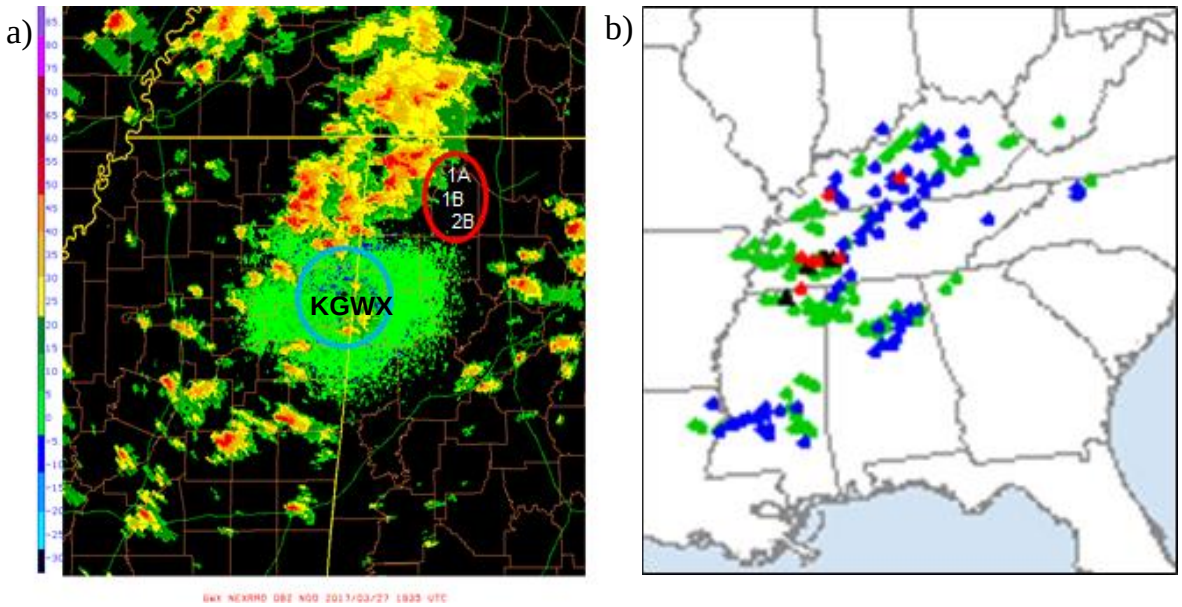

Figure 16 (a) is KGWX radar reflectivity on 27 March 2017 at 1935 UTC as cells approach PIPS 1A, PIPS 1B, and PIPS 2B (image adapted from http://catalog.eol.ucar.edu/vortex-se_2017/radar/113/1192/188087/54137971). Red and blue circles denote PIPS and KGWX locations, respectively. SPC (b) filtered storm report for 03/27/17. Red are tornado reports, blue are high wind reports, and green are hail reports (image adapted from www.spc.noaa.gov/exper/archive/event.php?date=20170327).

A radiosonde released over Haleyville, AL at 1924 UTC produced the skew-T log-P diagram (Fig. 17) to plot the vertical profiles of the atmosphere. The cluster had a small area of CIN between 850 mb and 800 mb followed by a narrow continuous region of CAPE, used to measure the updraft strength or severity of the storm. A multitude of reasons may have occurred due to no recorded sounding data beyond 470 mb; because of this, it displays no equilibrium level. The wind barbs show the change in wind speed and direction from the surface up to 470 mb, overall resulting in an increase in wind and a direction change from south southeast to southwest, represented by the hodograph (Fig. 18). The storm-relative winds at the surface are from the southeast and the 0-2 km storm-relative mean wind, represented by the purple line, is from the south southeast.

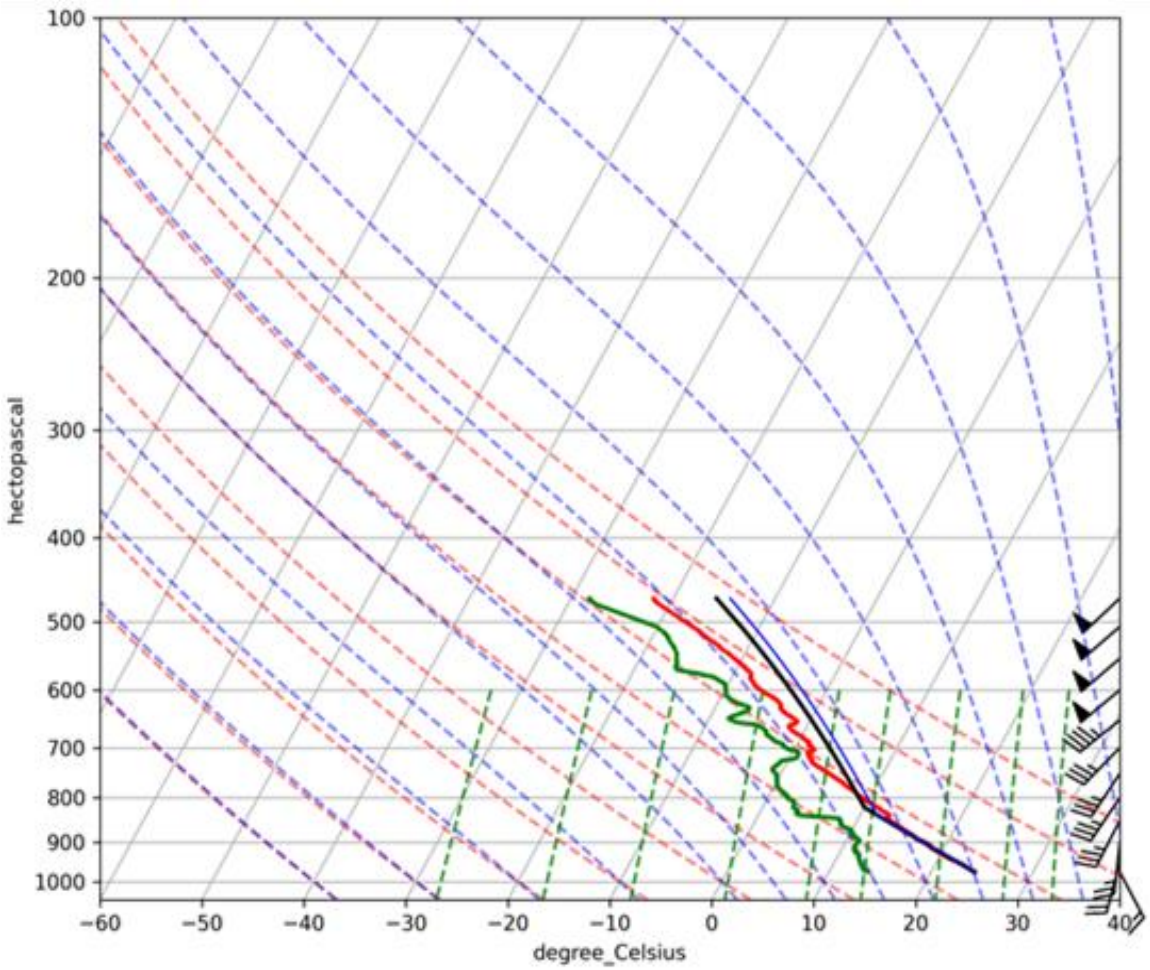

Figure 17. Skew-t chart produced from Haleyville, AL 1924 UTC radiosonde. Solid green line is T_d, solid red line is T, and the solid black line shows the parcels transition from the dry adiabatic lapse rate (DALR) to the saturated adiabatic lapse rate (SALR).

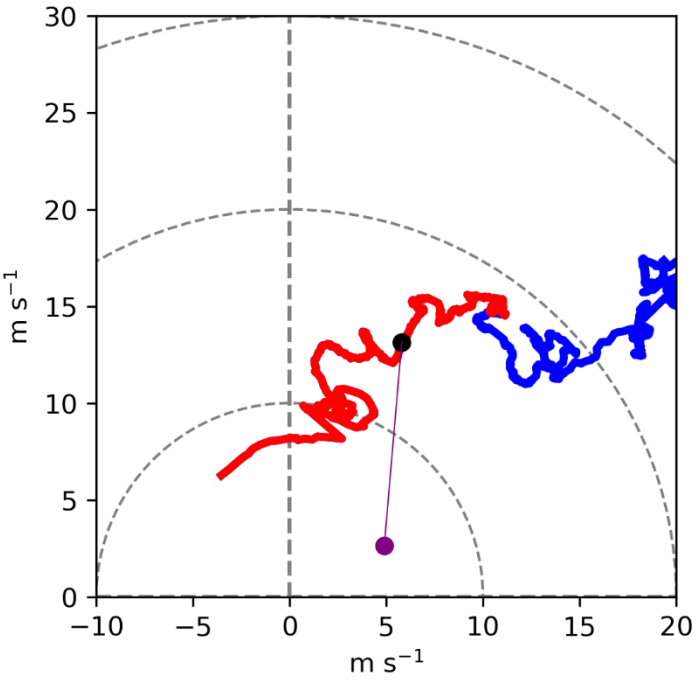

Figure 18. Haleyville, AL 1924 UTC VORTEX-SE hodograph sounding. The 0-2 km layer is in red, above 2 km layer in blue, the black dot represents the mean winds between the surface and 2 km, purple dot is the storm motion, and the purple line is the 0-2 km storm-relative mean wind vector.

Fig. 19, Fig. 20 and Fig. 21 is a time series of DSD (a) reflectivity and (b) differential reflectivity as different cells pass over PIPS 1A, PIPS 1B, and PIPS 2B, respectively. The largest cell passed over PIPS 1A, which was located farther north, with the maximum hydrometeor diameter occurring around 2040 UTC. PIPS 1B had a steady diameter distribution of hydrometeors between ~2110 UTC to ~2135 UTC. PIPS 2B encountered a weakening small cell with a lower number density and raindrop diameter.

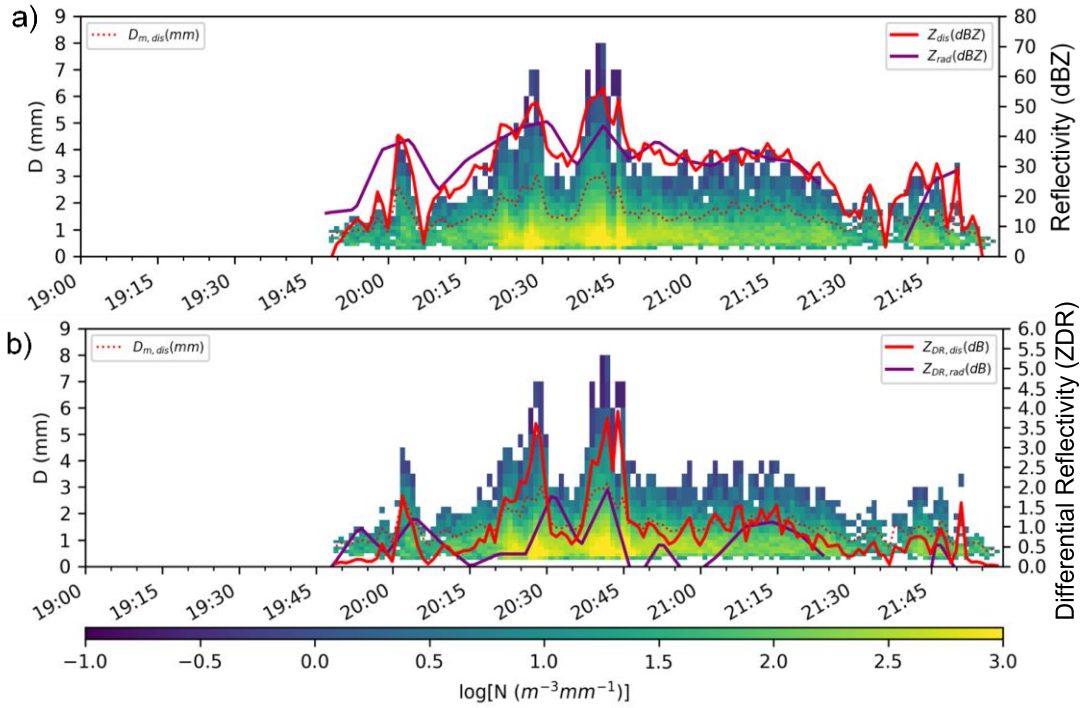

Figure 19. A time series of DSDs (a) reflectivity and (b) differential reflectivity from PIPS 1A (color shading is number density)

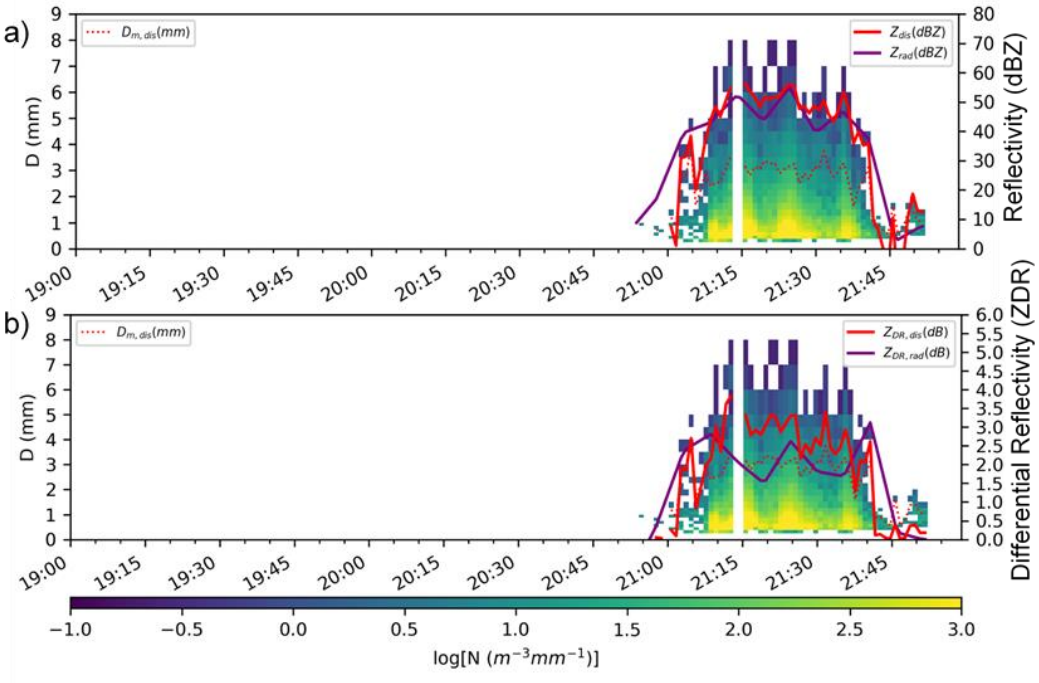

Figure 20. Same as Fig. 19 but at PIPS 1B.

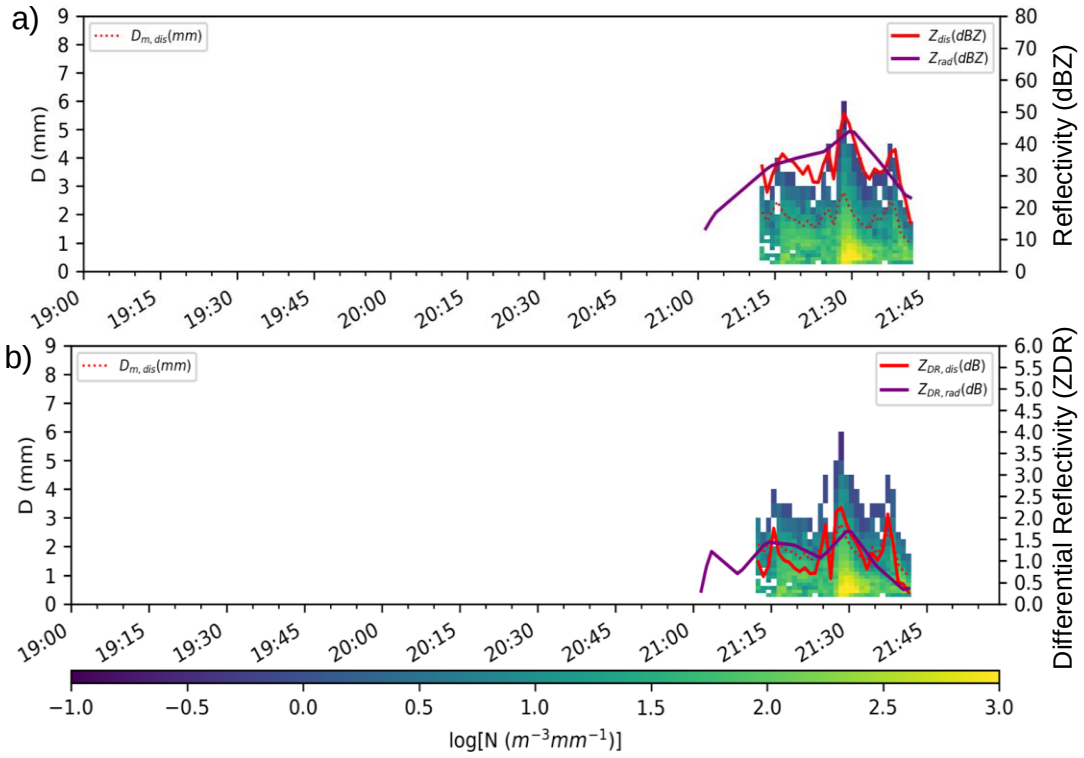

Figure 21. Same as Fig. 19 but at PIPS 2B.

Individual cells passed over each PIPS location, with the convective region of the first cell moving over PIPS 1A at ~1945 UTC, a second cell moving over PIPS 1B at ~2100 UTC, and a cell moving over PIPS 2B at ~2115 UTC. Figure 22 and 24 shows the gridded reflectivity and gridded differential reflectivity, respectively, at 2 km AGL as the earliest cell passed over PIPS 1A followed by a larger cell passing over PIPS 1B and PIPS 2B. Figure 23 and 25 shows the surface calculated reflectivity and surface calculated differential reflectivity, respectively, for PIPS 1A and for PIPS 1B and PIPS 2B, respectively. Each image was captured as the highest area of reflectivity passed over each PIPS location. The Z and Z_{DR} at the surface is greater than the Z and Z_{DR} at 2 km AGL.

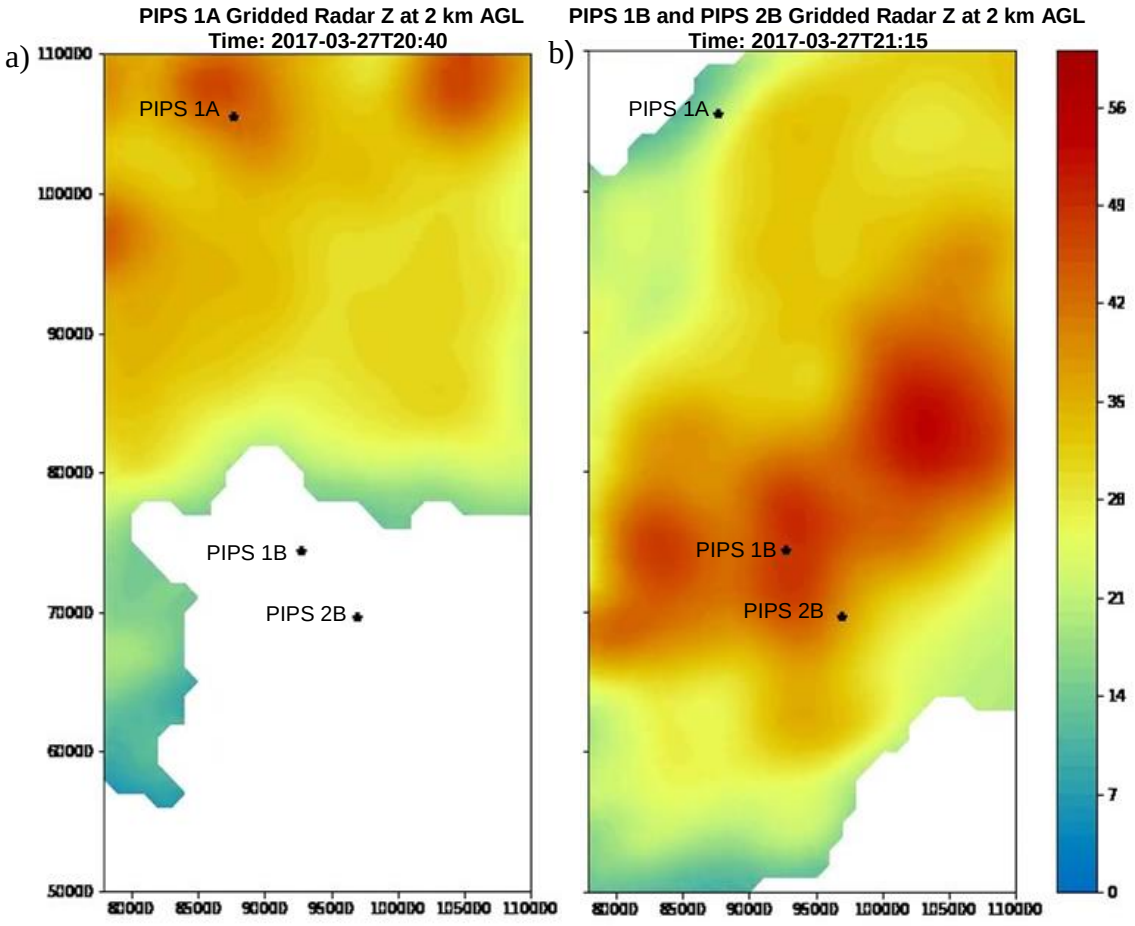

Figure 22. Time when the maximum gridded radar reflectivity at 2 km AGL was present at (a) PIPS 1A and (b) PIPS 1B and PIPS 2B.

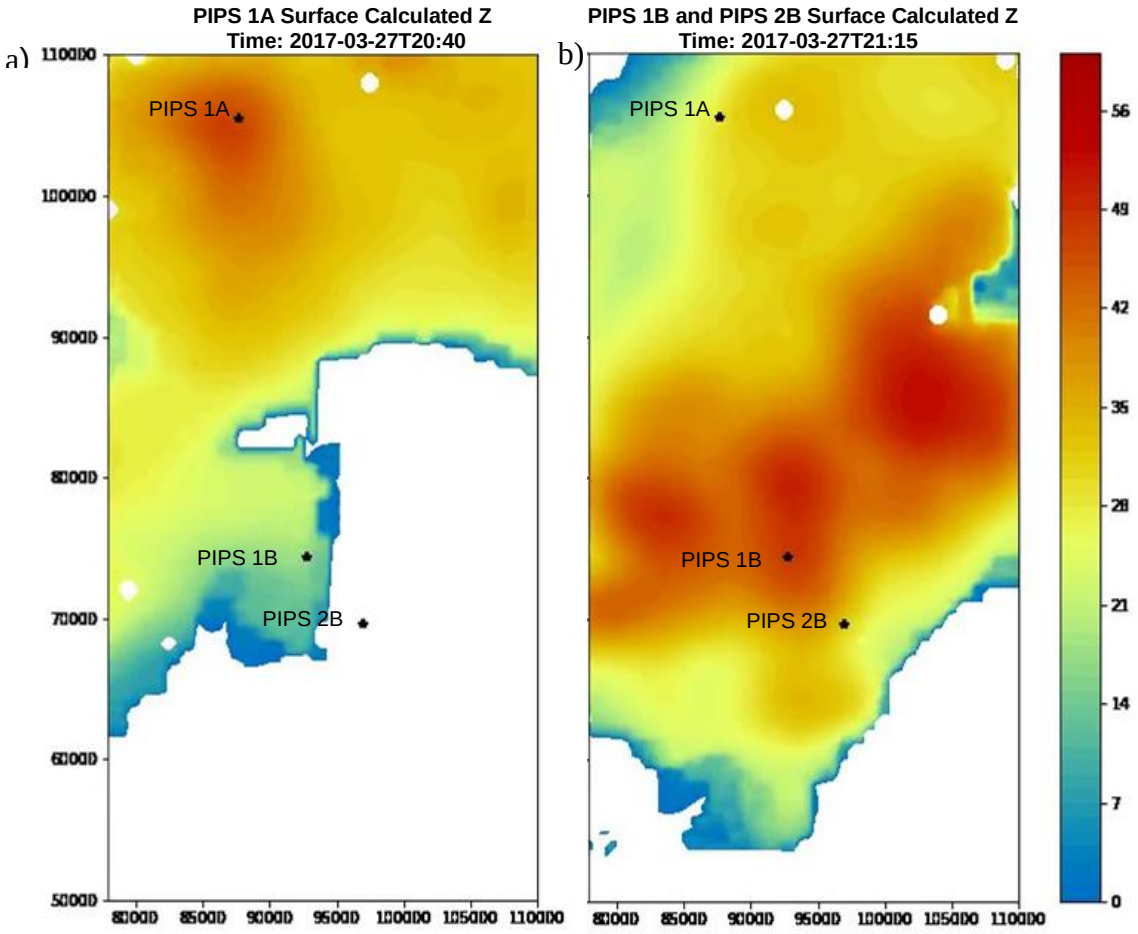

Figure 23. Same as Fig. 22 but with the surface calculated reflectivity.

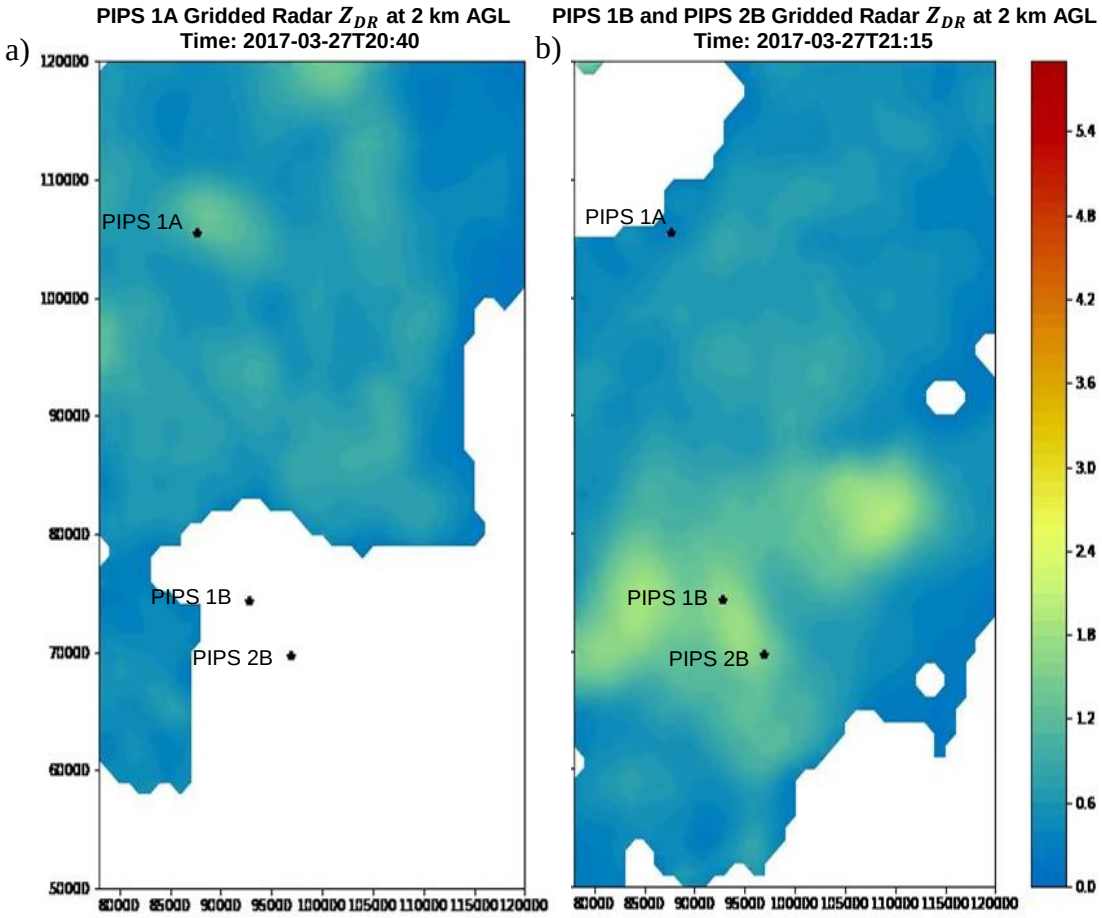

Figure 24. Same as Fig. 22 but with differential reflectivity.

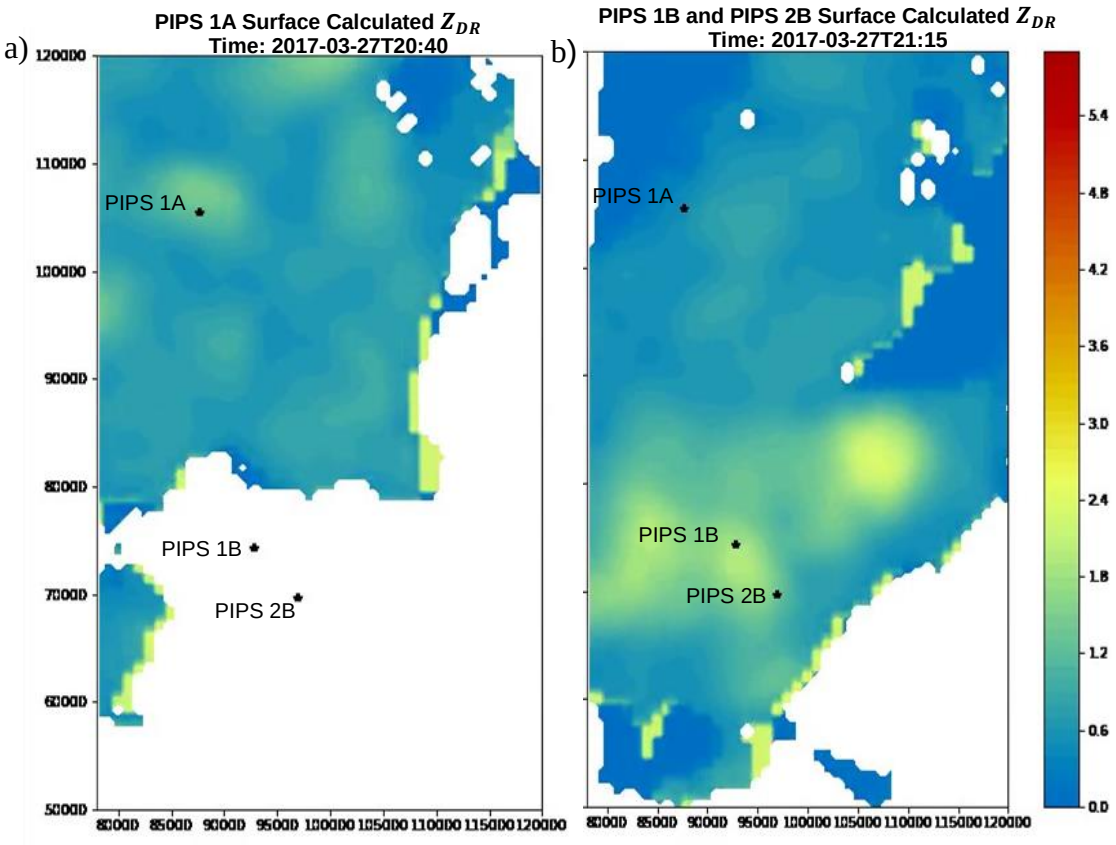

Figure 25. Same as Fig. 23 but with surface calculated differential reflectivity.

A time series of Z and Z_{DR} for each PIPS is shown in Figure 26 and 27, respectively. Overall, when comparing the peaks for Z, the derived surface sorted DSDs (blue) agrees better with the reflectivity derived from the surface PIPS-observed DSDs (black) than the reflectivity from both the original radar gate above the PIPS (purple) and the gridded and temporally interpolated radar data at 2 km AGL directly above the PIPS (green). Regarding Z_{DR} (Fig. 27), there is less agreement between the peaks of the derived surface sorted DSDs (blue) and the differential reflectivity derived from the surface PIPS-observed DSD (black). The reasons for the poor agreement in Z_{DR} for this case are unknown; possibilities include errors introduced by the gridding procedure and sampling errors in the disdrometer data.

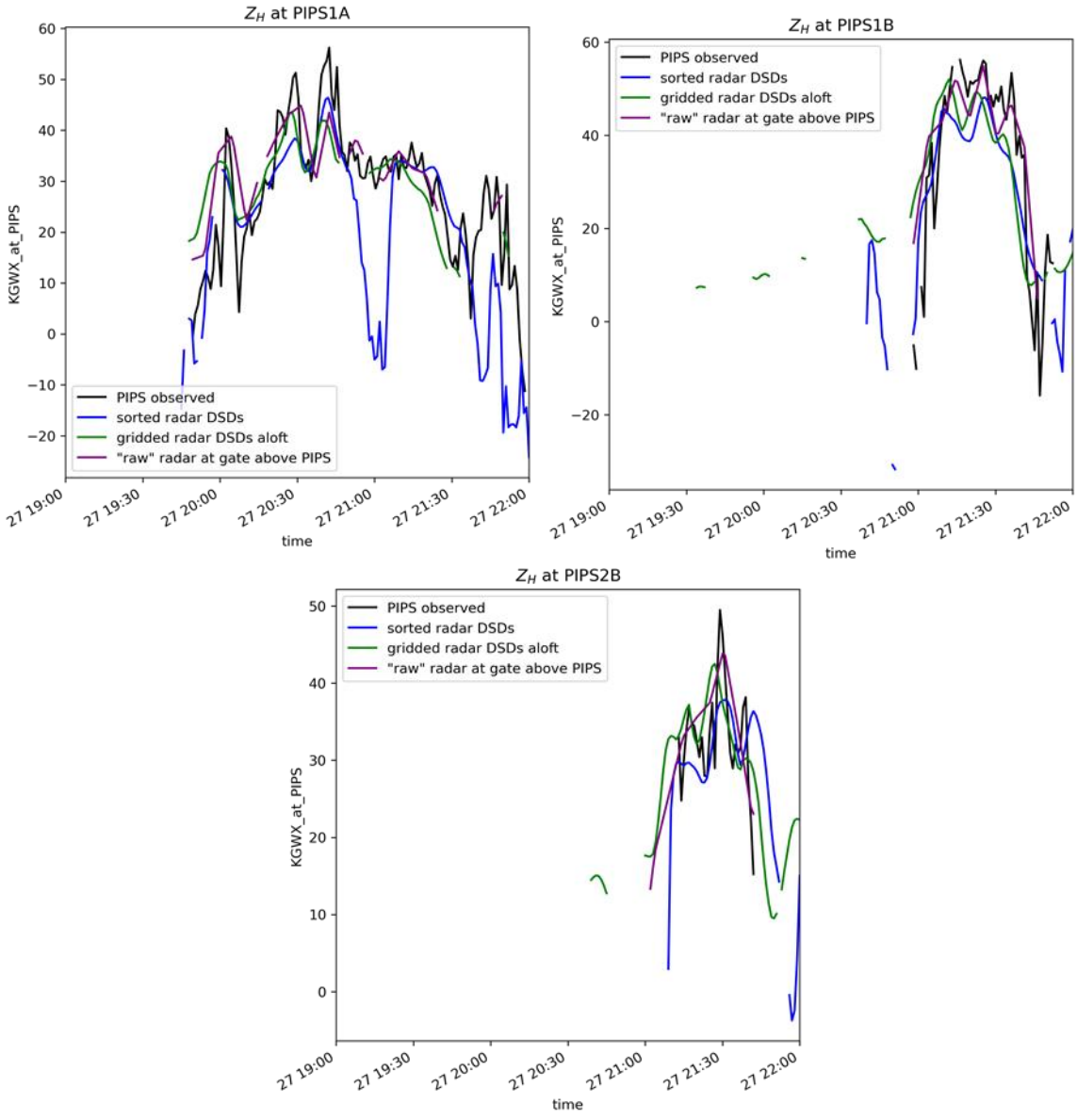

Figure 26. KGWX radar at PIPS 1A, PIPS 1B, and PIPS 2B versus reflectivity. Blue line is calculated from the size sorting model at the surface, green line is the gridded reflectivity at the top of the sorting layer (2 km AGL), purple line is the original raw radar data, and black line is the observed surface DSD derived from the PIPS.

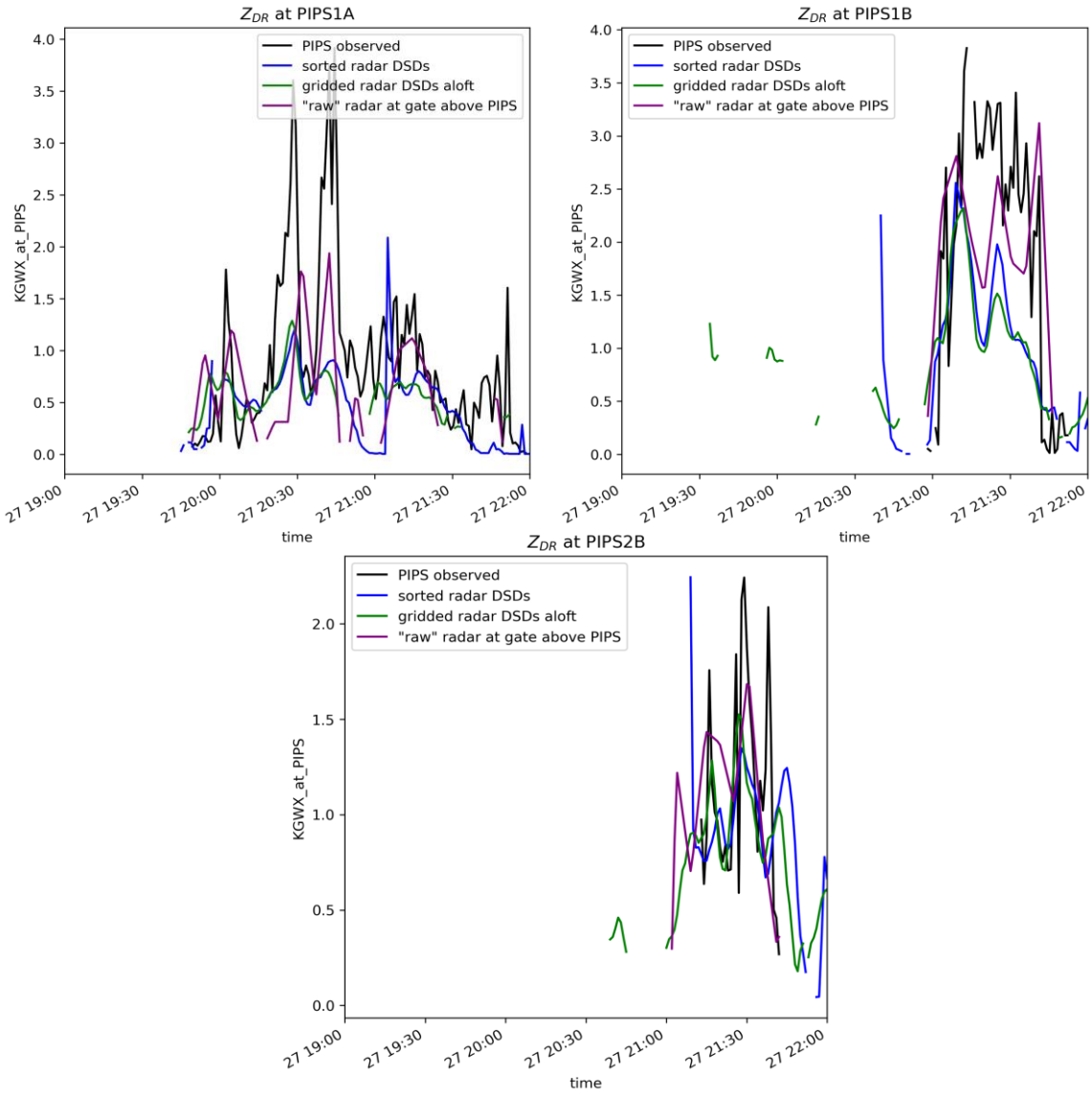

Figure 27. Same as Fig. 26 but for differential reflectivity.

5.1.3. 03/25/2017 IOP 1A

During the afternoon of 25 March 2017, the convective region of a nontornadic squall line with intermittent shear and rotation passed over PIPS 2B, PIPS 1B, and PIPS 1A sites from southwest to northeast, respectively. The convective region approached the PIPS location between ~1750 to ~1800 UTC. All PIPS were located in Lawrence County, Alabama and the closest WSR-88D radar was Columbus AFB, MS KGWX, located ~188 km southwest of all PIPS. The mean height of the radar beam over PIPS 2B, PIPS 1B, and PIPS 1A is 1805 m, 1855 m, and 2078 m,

respectively. A time series of DSD reflectivity and differential reflectivity as the squall line passes over PIPS 2B (Fig. 28), PIPS 1B (Fig. 29), and PIPS 1A (Fig. 30), respectively. Although PIPS 1A was located farther south and to the east, the storm motion was from the southwest and the convective region of the squall line bowed causing PIPS 2B and PIPS 1B to receive raindrops earlier. The PIPS vs. radar observed Z agree better than Z_{DR}, potentially due to the distance between the radar and the PIPS location.

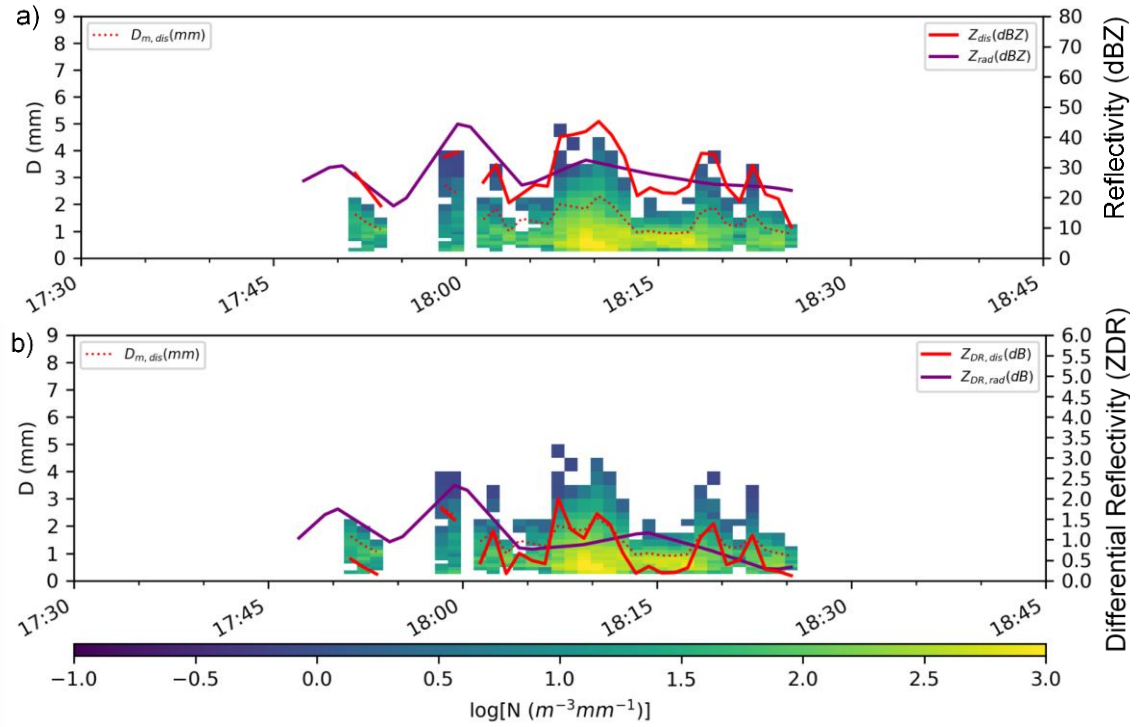

Figure 28. Time series of DSD (a) reflectivity and (b) differential reflectivity as the squall line passed over PIPS 2B. Red, purple, and red-dotted lines denote disdrometer-derived, radar-observed reflectivity, and mass-weighted mean diameter, respectively.

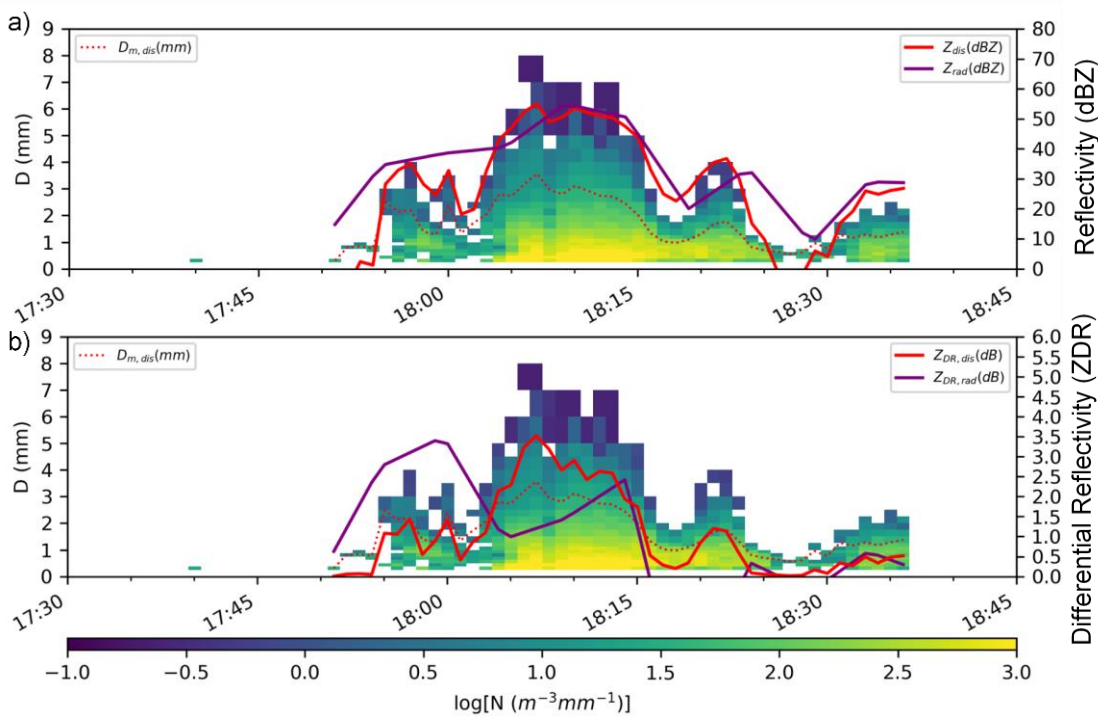

Figure 29. Same as Fig. 28 but at PIPS 1B.

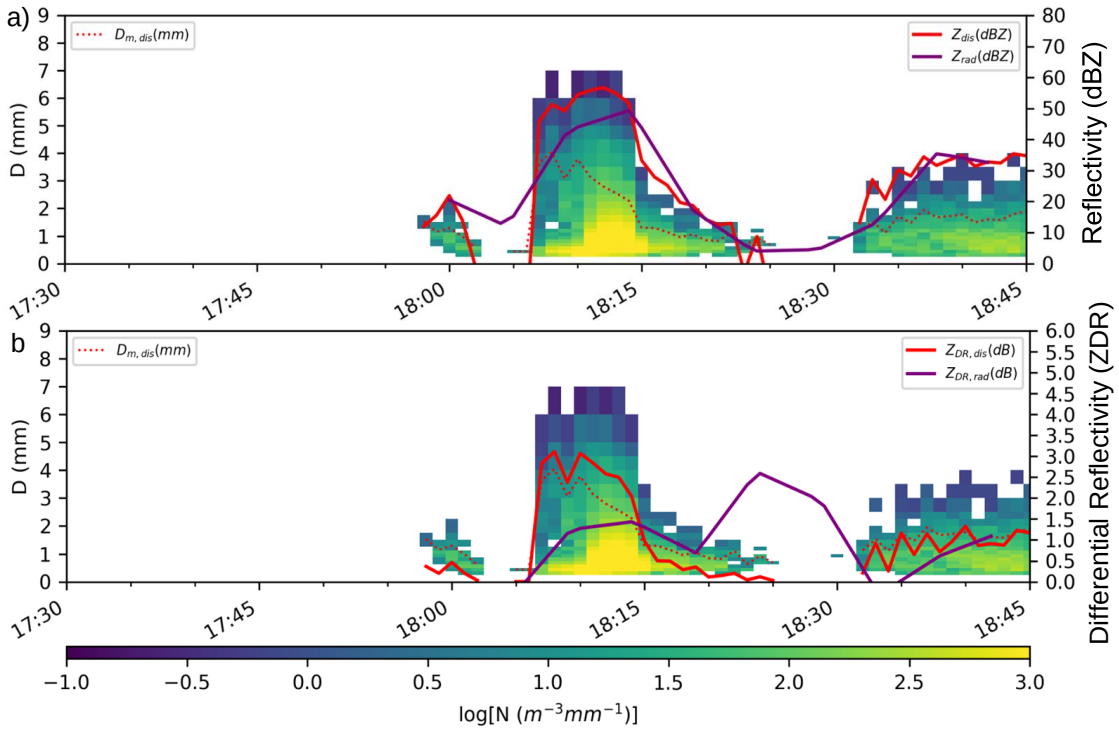

Figure 30. Same as Fig. 28 but at PIPS 1A.

A radiosonde released over Courtland, AL at 1759 UTC produced the skew-T log-P diagram (Fig. 31). Data from the sounding stopped at 530 mb. The sounding had a small area of CAPE between ~780 mb to ~600 mb, followed by the parcels reaching the equilibrium level, then entering another area of negative buoyancy. This shows that the squall line was not severe, at least compared to the previous two cases in this study. The wind barbs indicate the change in wind speed and direction from the surface up to 530 mb, overall resulting in an increase in winds and a small change in direction from south southwest, represented by the hodograph (Fig. 32). The storm-relative winds at the surface are from the north and the 0-2 km storm-relative mean wind, represented by the purple line, is from the south southeast.

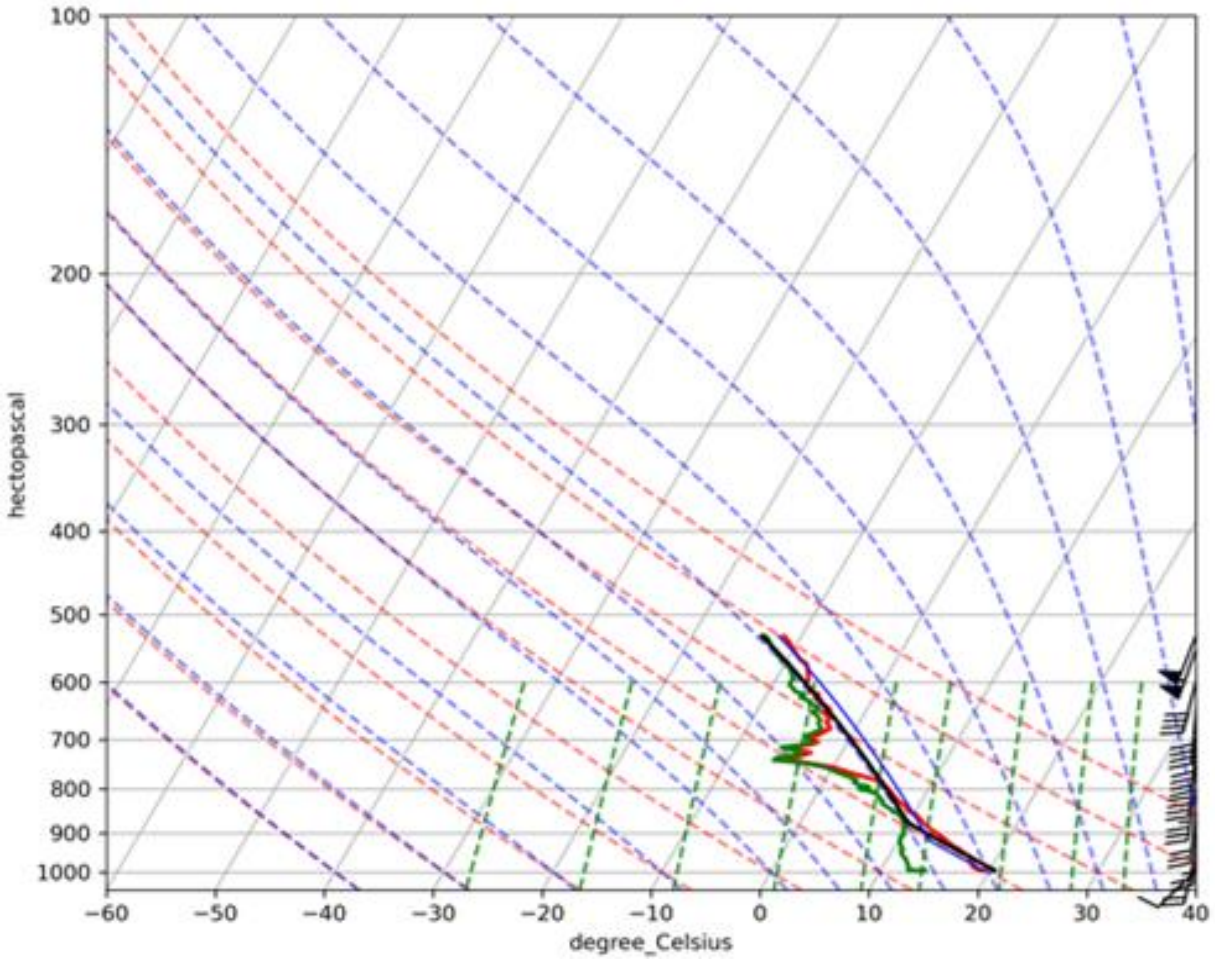

Figure 31. Same as Fig. 17 but using the Courtland, AL 1759 UTC radiosonde data for the PIPS locations on 03/25/2017.

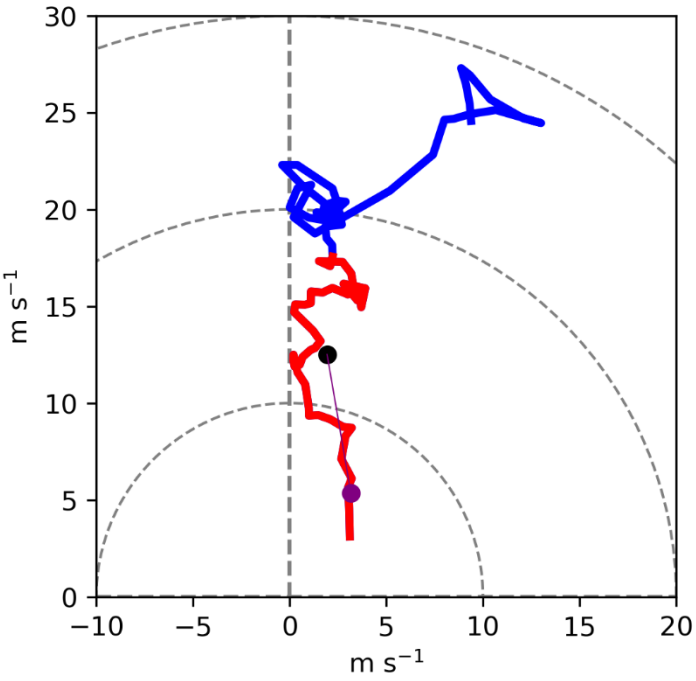

Figure 32. Same as Fig. 18 but using the Courtland, AL 1759 UTC radiosonde data for the PIPS locations on 03/25/2017.

At ~1813 UTC, the center of the squall line with the highest reflectivity passed over the PIPS locations. Although this case produce a short period of precipitation as compared to the previous cases, similarly, the surface calculated Z (Fig. 33b) and Z_{DR} (Fig. 34b) is stronger than the gridded Z (Fig. 33a) and Z_{DR} (Fig. 34a) at 2 km AGL.

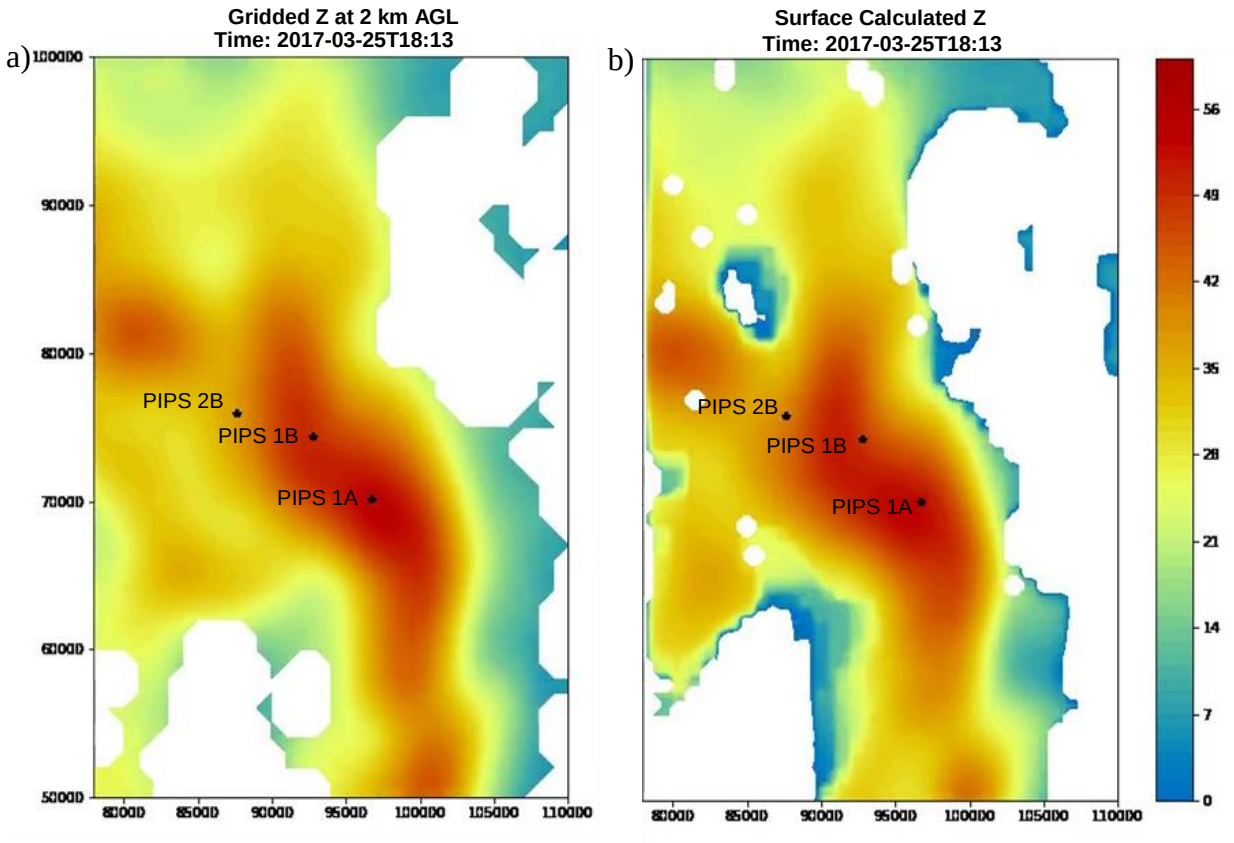

Figure 33. Gridded reflectivity (a) and surface calculated reflectivity (b) at PIPS 2B, PIPS 1B, and PIPS 1A for the 25 March 2017 case.

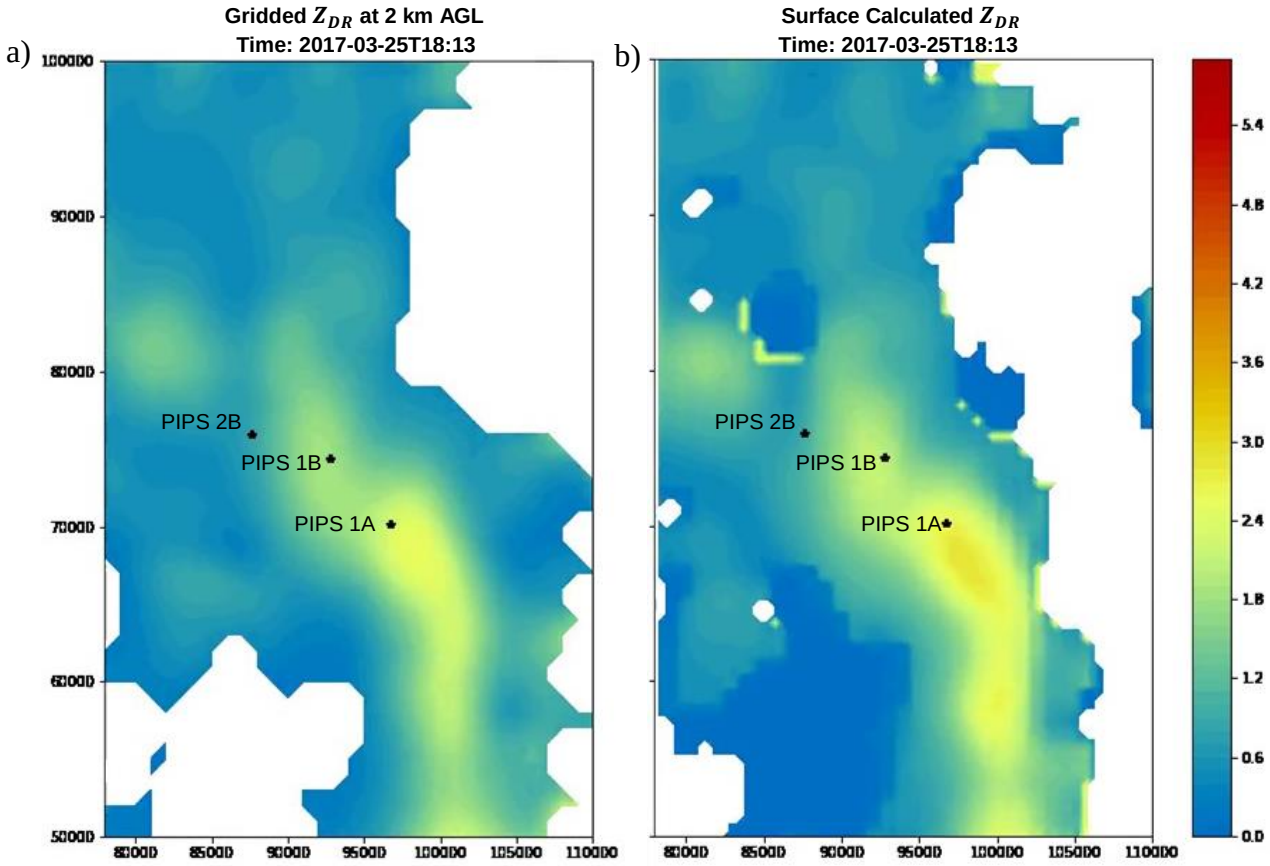

Figure 34. Same as Fig. 33 but for differential reflectivity.

The reflectivity time series (Fig. 35) is similar to the 27 March case. The overall peak comparison between the derived surface sorted DSDs agrees better with the reflectivity derived from the surface PIPS-observed DSDs than the reflectivity from both the original radar gate and the gridded interpolated radar above the PIPS. PIPS 1A comparison between the derived surface sorted DSD agrees better with the differential reflectivity derived from the surface PIPS-observed DSDs than the differential reflectivity from both the original radar gate and the gridded interpolated radar above the PIPS. The latter comparison does not show the same Z_{DR} agreement from PIPS 1B and PIPS 2B possibly due to the same reasons mentioned in the 27 March case.

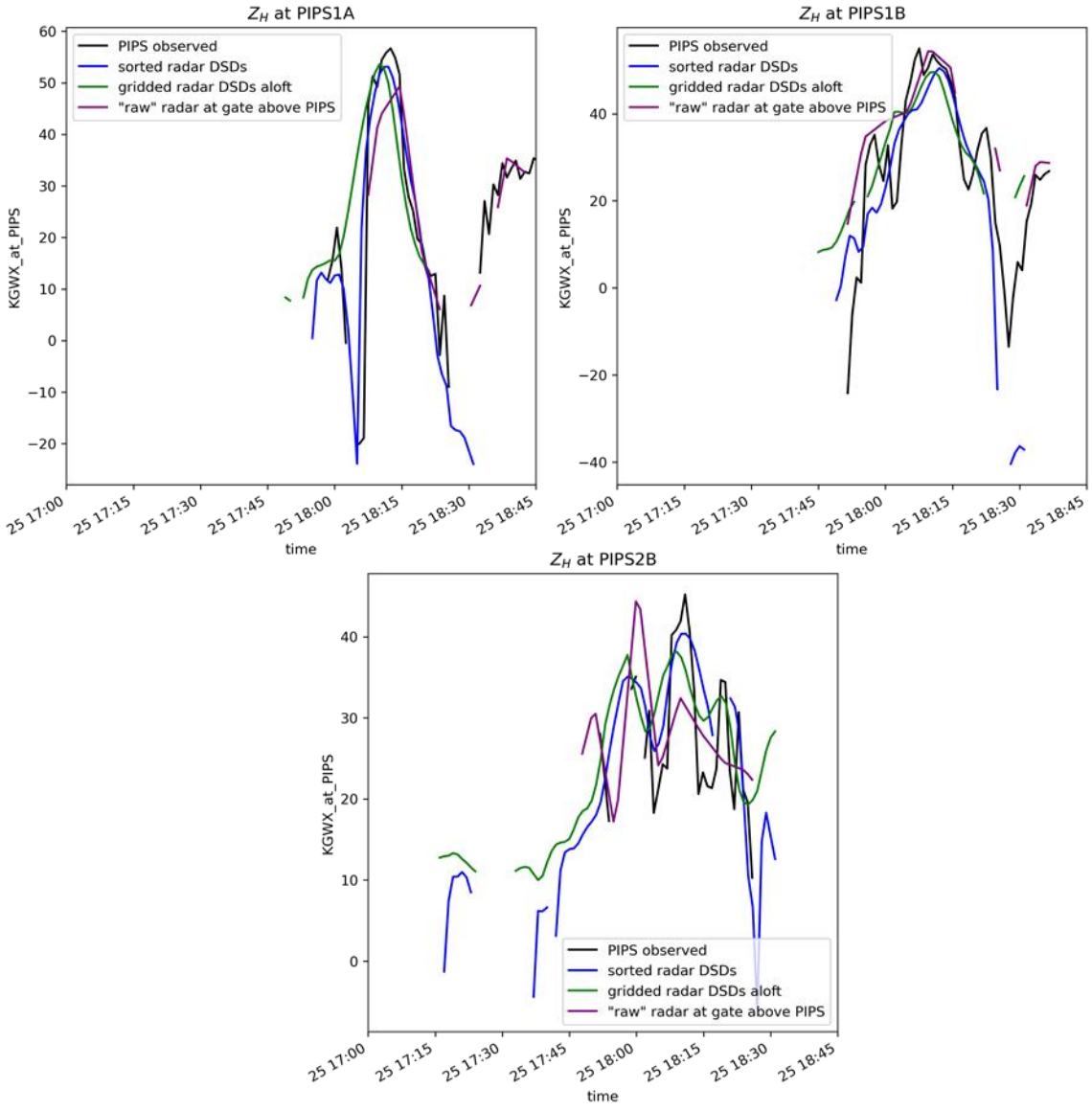

Figure 35. Same as Fig. 26 but for the 25 March 2017 case.

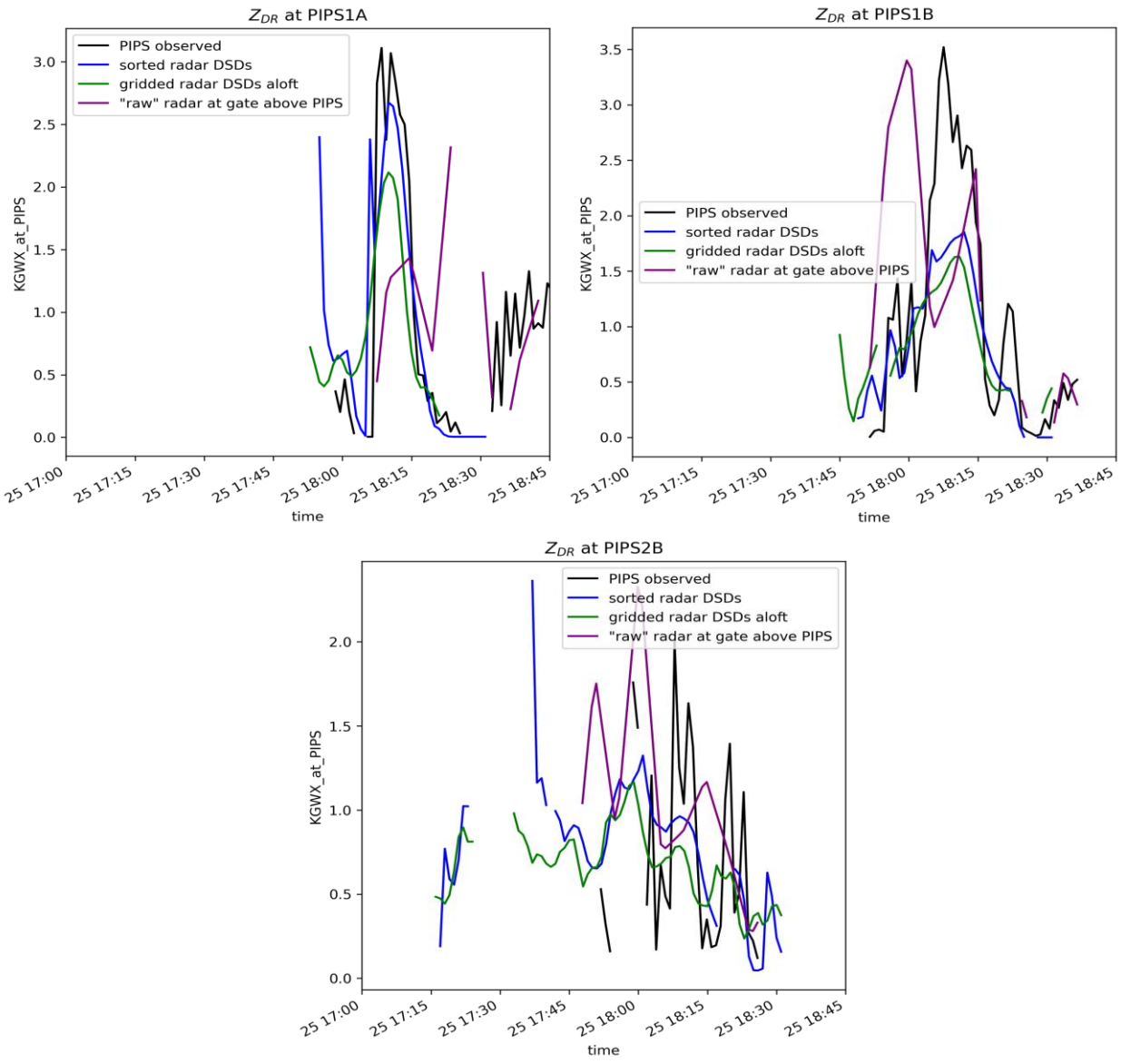

Figure 36. Same as Fig. 27 but for the 25 March 2017 case.

6. CONCLUSION AND FUTURE WORK

In this study, disdrometer data from the 2017 VORTEX-SE field program was analyzed and compared to radar observations relative to each case for the PIPS location. In reality, microphysical processes such as evaporation, collision, coalescence, and break up cause rain DSDs to vary in size but were neglected for simplicity. This analysis only examined size sorting due to storm-relative mean winds and neglected that due to transient effects and updrafts. Storm-relative winds can induce size sorting resulting in variable horizontal advection leading to a distinct horizontal spread of different drop sizes. The goal is to evaluate the impact of size sorting on DSD evolution from the radar level to the surface. Radar is often the only source of microphysical information aloft while disdrometers provide ground-truth surface measurements of DSDs. After retrieval of radar and disdrometer observations, the radar data is pre-processed and interpolated, applied to a trajectory model then the final DSDs are computed at the surface.

Three unique cases were used to investigate the results of radar and disdrometer DSD retrievals. We analyzed the 30 April case followed by the 25 March and 27 March case for comparison and to analyze the sorted radar DSDs at the surface. The horizontal spread of drops of different sizes shift as they fall towards the surface resulting from horizontal advection. Our trajectory model takes into account the change in the DSD due to size sorting and improves the agreement. Comparisons and analysis from the trajectory model derived from the discretized gamma distribution fits to observed radar data shows agreement in timing and magnitude of Z and Z_{DR} when compared to disdrometer observations of surface DSDs, specifically for the 30 April case. Z_{DR} shows less of an agreement than Z possibly due to errors introduced by the gridding procedure, sampling errors in the disdrometer data, and the fact that we neglected several microphysical processes, but this will require a more thorough investigation of the DSDs. The sorted radar DSDs at the surface are overall closer to the disdrometer observations than the original radar DSDs aloft. Results also show that the spatial variation of DSDs is higher at the surface due to size sorting by the storm-relative mean winds. This could be due to neglecting other microphysical processes listed above.

Future work will improve the trajectory model to allow more realistic inhomogeneous time-varying wind fields to investigate the importance of storm-scale circulations. Additionally, vertical profiles of retrieved DSDs from the FMCW radar will be examined in the context of the

size-sorting model. Plenty of data is not gathered beneath the lowest elevation scan of S-Band radars so incorporating a vertical profiling radar will narrow the loss data gap. Many storms mature farther away from radars, as with the 25 March and 27 March cases. As part of the motivation for this study, we want to mitigate the effects of being far from the radar by taking into account the DSD evolution below the radar horizon. Minimized distance between disdrometer locations and radars will provide better data comparison due to lower radar elevation scans closer to the radar. This is a likely reason the 30 April case has a better agreement than the other two cases. Also, launching mobile radiosondes within a reasonable time frame ahead of the storm would provide more accurate and representative near-storm wind profiles. Methods will need continued modification to improve the Z_{DR} agreement in timing and magnitude between the sorted DSDs at the surface from the trajectory model and the disdrometer observations derived from the PIPS.

REFERENCES

Ashley, W. S., Krmenec, A. J., and Schwantes, R., (2008). Vulnerability due to Nocturnal Tornadoes, *Weather and Forecasting, 23(5),* 795-807.

Battan, L. J., (1977). Rain Resulting from Melting Ice Particles. *Journal of Applied Meteorology, 16(6),* 595–604.

Brandes, E. A., Zhang, G., and Vivekanandan, J., (2002). Experiments in Rainfall Estimation with a Polarimetric Radar in a Subtropical Environment. *Journal of Applied Meteorology, 41(6),* 674–685.

——, ——, and ——, (2003). An Evaluation of a Drop Distribution–Based Polarimetric Radar Rainfall Estimator. *Journal of Applied Meteorology, 42(5),* 652–660.

——, ——, and ——, (2004a). Drop Size Distribution Retrieval with Polarimetric Radar: Model and Application. *Journal of Applied Meteorology, 43(3),* 461–475.

——, ——, and ——, (2004b). Comparison of Polarimetric Radar Drop Size Distribution Retrieval Algorithms. *Journal of Atmospheric and Oceanic Technology, 21(4),* 584–598.

Brown, M., (2018). MSU Mobile Radiosonde Data. Version 1.1. UCAR/NCAR - Earth Observing Laboratory. https://doi.org/10.5065/D6H70DKK.

Cao, Q., Zhang, G., Brandes, E., Schuur, T., Ryzhkov, A. and Ikeda, K., (2008). Analysis of Video Disdrometer and Polarimetric Radar Data to Characterize Rain Microphysics in Oklahoma. *Journal of Applied Meteorology and Climatology, 47(8),* 2238-2255.

—— and ——, (2009). Errors in Estimating Raindrop Size Distribution Parameters Employing Disdrometer and Simulated Raindrop Spectra. *Journal of Applied Meteorology and Climatology, 48(2),* 406–425.

Dawson, D., Mansell, E. and Kumjian, M., (2014). Does Wind Shear Cause Hydrometeor Size Sorting?. *Journal of the Atmospheric Sciences, 72(1),* 340-348.

——, Xue, M., Milbrandt, J. A., and Shapiro, A., (2015). Sensitivity of Real-Data Simulations of the 3 May 1999 Oklahoma City Tornadic Supercell and Associated Tornadoes to Multimoment Microphysics. Part I: Storm- and Tornado-Scale Numerical Forecasts. *Monthly Weather Review*, *143*(6), 2241–2265.

——, Biggerstaff, M., and Waugh, S., (2020). Purdue University Portable In Situ Precipitation Stations (PIPS) Data. Version 1.0. UCAR/NCAR - Earth Observing Laboratory.

Earth Observing Laboratory, (2020). Purdue University Portable in Situ Precipitation Stations (PIPS) Data. [Available online at https://data.eol.ucar.edu/dataset/541.029].

Fang, F., (2003). Raindrop Size Distribution Retrieval and Evaluation Using an S-Band Radar Profiler.

Friedrich, K., Kalina, E. A., Masters, F. J., and Lopez, C. R., (2013). Drop-Size Distributions in Thunderstorms Measured by Optical Disdrometers during VORTEX2. *Monthly Weather Review, 141(4),* 1182–1203.

——, Higgins, S., Masters, F. J., and Lopez, C. R., (2013). Articulating and Stationary PARSIVEL Disdrometer Measurements in Conditions with Strong Winds and Heavy Rainfall. *Journal of Atmospheric and Oceanic Technology, 30(9),* 2063-2080.

Griffin, S., Otkin, J., Thompson, G., Frediani, M., Berner, J. and Kong, F., (2020). Assessing the Impact of Stochastic Perturbations in Cloud Microphysics using GOES-16 Infrared Brightness Temperatures. *Monthly Weather Review, 148(8),* 3111-3137.

Gunn, R. E., and Marshall, J. S., (1955). The Effect of Wind Shear on Falling Precipitation. *Journal of Meteorology, 12(4),* 339–349.

Helmus, J. J., and Collis, S. M., (2016). The Python ARM Radar Toolkit (Py-ART), a Library for Working with Weather Radar Data in the Python Programming Language. *Journal of Open Research Software, 4(1),* p.e25.

Islam, T., Rico-Ramirez, M. A., Han, D.,and Srivastava, P. K., (2012). A Joss-waldvogel Disdrometer Derived Rainfall Estimation Study by Collocated Tipping Bucket and Rapid Response Rain Gauges. *Atmospheric Science Letters, 13(2),* 139–150.

Jameson, A. R., and Kostinski, A. B., (2001). What is a Raindrop Size Distribution? *Bulletin of the American Meteorological Society, 82,* 1169–1178.

Joss, J., and Waldvogel, A., (1969). Raindrop Size Distribution and Sampling Size Errors. *Journal of the Atmospheric Sciences, 26(3),* 566–569.

Jung, Y., Xue, M., and Zhang, G., (2010). Simulations of Polarimetric Radar Signatures of a Supercell Storm Using a Two-moment Bulk Microphysics Scheme. *Journal of Applied Meteorology and Climatology, 49,* 146-163.

Klemp, J., (1987). Dynamics of Tornadic Thunderstorms. *Annual Review of Fluid Mechanics, 19(1),* 369-402.

Kliche, D. V., Smith, P. L., and Johnson, R. W., (2008). L-Moment Estimators as Applied to Gamma Drop Size Distributions. *Journal of Applied Meteorology and Climatology, 47(12),* 3117–3130.

Kluyver, T., Ragan-Kelley, B., Perez, F., Granger, B., Bussonnier, M., Frederic, J., Kelley, K., Hamrick, J., Grout, J., Corlay, S., Ivanov, P., Damian, A., Abdalla, S., and Willing, C., (2016). Jupyter Notebooks – A Publishing Format for Reproducible Computational Workflows. In F. Loizides & B. Schmidt (Eds.), *Positioning and Power in Academic Publishing: Players, Agents and Agendas*, 87–90.

Kollias, P., Albrecht, B. and Marks, F., (2001). Raindrop Sorting Induced by Vertical Drafts in Convective Clouds. *Geophysical Research Letters, 28(14),* 2787-2790.

Kozu, T., Iguchi, T., Shimomai, T. and Kashiwagi, N., (2009). Raindrop Size Distribution Modeling from a Statistical Rain Parameter Relation and Its Application to the TRMM Precipitation Radar Rain Retrieval Algorithm. *Journal of Applied Meteorology and Climatology, 48(4),* 716-724.

Kruger, A. and Krajewski, W., (2002). Two-Dimensional Video Disdrometer: A Description. *Journal of Atmospheric and Oceanic Technology, 19(5),* 602-617.

Kumjian, M. R. and Ryzhkov, A. V., (2009). Storm-Relative Helicity Revealed from Polarimetric Radar Measurements. *Journal of the Atmospheric Sciences, 66(3),* 667–685.

—— and ——. (2012). The Impact of Size Sorting on the Polarimetric Radar Variables. *Journal of the Atmospheric Sciences, 69(6),* 2042-2060.

Laws, J. and Parsons, D., (1943). The Relation of Raindrop-Size to Intensity. *Transactions, American Geophysical Union, 24(2),* 452.

Löffler-Mang, M., and Joss, J., (2000). An Optical Disdrometer for Measuring Size and Velocity of Hydrometeors. *Journal of Atmospheric and Oceanic Technology, 17(2),* 130-139.

Mahale, V. N., Brotzge, J. A., and Bluestein, H. B., (2012). An Analysis of Vortices Embedded within a Quasi-Linear Convective System Using X-Band Polarimetric Radar. *Weather and Forecasting, 27(6),* 1520–1537.

Moisseev, D. N., and Chandrasekar, V., (2007). Examination of the μ–Λ Relation Suggested for Drop Size Distribution Parameters. *Journal of Atmospheric and Oceanic Technology, 24(5),* 847-855.

Morrison, H., Kumjian, M., Martinkus, C., Prat, O., and Van Lier-Walqui, M. (2019). A General N-Moment Normalization Method for Deriving Raindrop Size Distribution Scaling Relationships. *Journal of Applied Meteorology and Climatology, 58(2),* 247-267.

NCEI Radar Data, (2020). NEXRAD data archive, inventory, and access. [Available online at https://www.ncdc.noaa.gov/nexradinv/].

NWS Huntsville, Alabama, (2020). Damaging winds and an isolated tornado on April 30, 2017. [Available online at https://www.weather.gov/hun/event_043017].

NWS Storm Prediction Center. [Available online at https://www.spc.noaa.gov/].

——, (2020). Severe Weather Event: Monday March 27, 2017. [Available at https://www.spc.noaa.gov/exper/archive/event.php?date=20170327].

——, (2020). Severe weather event: April 30, 2017. [Available online at https://www.spc.noaa.gov/exper/archive/event.php?date=20170430].

Ohtake, T., (1970). Factors Affecting the Size Distribution of Raindrops and Snowflakes. *Journal of the Atmospheric Sciences, 27(5),* 804-813.

Peters, G., Fischer, B., Münster, H., Clemens, M. and Wagner, A., (2005). Profiles of Raindrop Size Distributions as Retrieved by Microrain Radars. *Journal of Applied Meteorology, 44(12),* 1930-1949.

Porcù, F., D'Adderio, L., Prodi, F. and Caracciolo, C., (2013). Effects of Altitude on Maximum Raindrop Size and Fall Velocity as Limited by Collisional Breakup. *Journal of the Atmospheric Sciences, 70(4),* 1129-1134.

Pulkkinen, S., Nerini, D. Perez Hortal. A., Velasco-Forero, C., Germann, U., Seed, A., and Foresti, L., (2019). Pysteps: An Open-source Python Library for Probabilistic Precipitation Nowcasting (v1.0). *Geoscientific Model Development. 12 (10),* 4185–4219.

Rasmussen, E., (2015). VORTEX-Southeast Program Overview. *National Severe Storms Laboratory,* 1–36.

Rauber, R. M., Beard, K. V., and Andrews, B. M., (1991). A Mechanism for Giant Raindrop Formation in Warm, Shallow Convective Clouds. *Journal of the Atmospheric Science*s, *48*, 1791–1797.

——, and S. W. Nesbitt, (2018). Radar Meteorology: A First Course. Wiley Blackwell, 461.

Rigby, E., Marshall, J., and Hitschfeld, W., (1954). The Development of the Size Distribution of Raindrops during Their Fall. *Journal of Meteorology, 11(5),* 362-372.

Rocadenbosch, F., Barragan, R., Frasier, S. J., Waldinger, J., Turner, D. D., Tanamachi, R. L., and Dawson, D. T., (2020). Ceilometer-Based Rain-Rate Estimation: A Case-Study Comparison with S-Band Radar and Disdrometer Retrievals in the Context of VORTEX-SE. *IEEE Transactions on Geoscience and Remote Sensing, 58(12),* 8268–8284.

Schuur, T., Ryzhkov, A., Zrnić, D. and Schönhuber, M., (2001). Drop Size Distributions Measured by a 2D Video Disdrometer: Comparison with Dual-Polarization Radar Data. *Journal of Applied Meteorology, 40(6),* 1019-1034.

Smith, P. L., (2003). Raindrop Size Distributions: Exponential or Gamma—Does the Difference Matter? *Journal of Applied Meteorology, 42(7),* 1031-1034.

——, and Kliche, D. V., (2005). The Bias in Moment Estimators for Parameters of Drop Size Distribution Functions: Sampling from Exponential Distributions, *Journal of Applied Meteorology, 44(8),* 1195-1205.

Testud, J., Oury, S., Black, R. A., Amayenc, P., and Dou, X., (2001). The Concept of "Normalized" Distribution to Describe Raindrop Spectra: A Tool for Cloud Physics and Cloud Remote Sensing, *Journal of Applied Meteorology, 40(6),* 1118-1140.

Thurai, M., Petersen, W., Tokay, A., Schultz, C. and Gatlin, P., (2011). Drop Size Distribution Comparisons between Parsivel and 2-D Video Disdrometers. *Advances in Geosciences, 30,* 3-9.

Tridon, F., Battaglia, A., Luke, E. and Kollias, P., (2017). Rain Retrieval from Dual-Frequency Radar Doppler Spectra: Validation and Potential for a Midlatitude Precipitating Case-Study. *Quarterly Journal of the Royal Meteorological Society, 143(704),* 1364-1380.

Tokay, A., Kruger, A., and Krajewski, W., (2001). Comparison of Drop Size Distribution Measurements by Impact and Optical Disdrometers. *Journal of Applied Meteorology, 40(11),* 2083–2097.

——, Petersen, W. A., Gatlin, P., and Wingo, M., (2013). Comparison of Raindrop Size Distribution Measurements by Collocated Disdrometers. *Journal of Atmospheric and Oceanic Technology, 30(8),* 1672–1690.

——, Wolff, D. B., and Petersen, W. A., (2014). Evaluation of the New Version of the Laser-Optical Disdrometer, OTT Parsivel2. *Journal of Atmospheric and Oceanic Technology, 31(6),* 1276–1288.

Uijlenhoet, R., and Pomeroy, J. H., (2001). Raindrop Size Distributions and Radar Reflectivity? Rain Rate Relationships for Radar Hydrology. *Hydrology and Earth System Sciences, 5(4),* 615-628.

Ulbrich, C., (1983). Natural Variations in the Analytical Form of the Raindrop Size Distribution. *Journal of Climate and Applied Meteorology, 22(10),* 1764-1775.

——, (1985). The Effects of Drop Size Distribution Truncation on Rainfall Integral Parameters and Empirical Relations. *Journal of Climate and Applied Meteorology*, *24(6)*, 580-590.

——, and Atlas, D., (1998). Rainfall Microphysics and Radar Properties: Analysis Methods for Drop Size Spectra. *Journal of Applied Meteorology, 37(9)*, 912-923.

Understanding Weather Radar, (2021): Weather Underground. [Available at https://www.wunderground.com/prepare/understanding-radar].

US Department of Commerce, N. O. A. A., (2021). Alabama Tornado Statistics. *National Weather Service*. NOAA's National Weather Service. [Available online at https://www.weather.gov/bmx/tornadostats2].

Vivekanandan, J., Adams, W. and Bringi, V., (1991). Rigorous Approach to Polarimetric Radar Modeling of Hydrometeor Orientation Distributions. *Journal of Applied Meteorology*, *30(8)*, 1053-1063.

——, Zhang, G. and Brandes, E., (2004). Polarimetric Radar Estimators Based on a Constrained Gamma Drop Size Distribution Model. *Journal of Applied Meteorology*, *43(2)*, 217-230.

VORTEX Southeast. NOAA National Severe Storms Laboratory. [Available online at http://www.nssl.noaa.gov/projects/vortexse/].

VORTEX-SE 2017 Field Catalog. VORTEX-SE_2017 Field Catalog | NCAR EOL. [Available online at http://catalog.eol.ucar.edu/vortex-se_2017/tools/missions].

Wallace, J. M., and Hobbs, P. V., (2011). Atmospheric Science: An Introductory Survey. Amsterdam: Elsevier Acad. Press.

Williams, C., Beauchamp, R. and Chandrasekar, V., (2016). Vertical Air Motions and Raindrop Size Distributions Estimated Using Mean Doppler Velocity Difference From 3- and 35-GHz Vertically Pointing Radars. *IEEE Transactions on Geoscience and Remote Sensing*, *54(10)*, 6048-6060.

Wong, R. and Chidambaram, N., (1985). Gamma Size Distribution and Stochastic Sampling Errors. *Journal of Climate and Applied Meteorology*, *24(6)*, 568-579.

Wu, W., Zou, H., Shan, J. and Wu, S., (2018). A Dynamical Z-R Relationship for Precipitation Estimation Based on Radar Echo-Top Height Classification. *Advances in Meteorology*, 1-11.

Zhang, G., Vivekanandan, J., Brandes, E., (2001). A Method for Estimating Rain Rate and Drop Size Distribution from Polarimetric Radar Measurements. *IEEE Transactions on Geoscience and Remote Sensing, 39(4)*, 830–841.

——, ——, ——, Meneghini, R. and Kozu, T., (2003). The Shape–Slope Relation in Observed Gamma Raindrop Size Distributions: Statistical Error or Useful Information? *Journal of Atmospheric and Oceanic Technology*, *20(8)*, 1106-1119.

——, Xue, M., Cao, Q., and Dawson, D. T., (2008). Diagnosing the Intercept Parameter for Exponential Raindrop Size Distribution Based on Video Disdrometer Observations: Model Development. *Journal of Applied Meteorology and Climatology, 47(11)*, 2983–2992.